St. John's University
St. John's Scholar

Theses and Dissertations

2021

PARTICLE SHAPE ENGINEERING FOR IMPROVED DRUG DELIVERY TO PERIPHERAL LUNGS BY NON-INVASIVE ROUTE

Snehal Shukla
Saint John's University, Jamaica New York

Follow this and additional works at: https://scholar.stjohns.edu/theses_dissertations

 Part of the Pharmacy and Pharmaceutical Sciences Commons

Recommended Citation

Shukla, Snehal, "PARTICLE SHAPE ENGINEERING FOR IMPROVED DRUG DELIVERY TO PERIPHERAL LUNGS BY NON-INVASIVE ROUTE" (2021). *Theses and Dissertations*. 301.
https://scholar.stjohns.edu/theses_dissertations/301

This Dissertation is brought to you for free and open access by St. John's Scholar. It has been accepted for inclusion in Theses and Dissertations by an authorized administrator of St. John's Scholar. For more information, please contact fazzinol@stjohns.edu.

www.manaraa.com

PARTICLE SHAPE ENGINEERING FOR IMPROVED DRUG DELIVERY
TO PERIPHERAL LUNGS BY NON-INVASIVE ROUTE

A dissertation submitted in partial fulfillment
of the requirements for the degree of

DOCTOR OF PHILOSOPHY

to the faculty of the

DEPARTMENT OF PHARMACEUTICAL SCIENCES

of

COLLEGE OF PHARMACY AND HEALTH SCIENCES

at

ST. JOHN'S UNIVERSITY
New York
by
Snehal Shukla

Date Submitted _____ Date Approved _____

_____ _____

Snehal Shukla Dr. Vivek Gupta

www.manaraa.com

© Copyright by Snehal Shukla 2021

All Rights Reserved

www.manaraa.com

ABSTRACT

PARTICLE SHAPE ENGINEERING FOR IMPROVED DRUG DELIVERY TO PERIPHERAL LUNGS BY NON-INVASIVE ROUTE

Snehal Shukla

Inhalation of therapeutics has been gaining importance owing to immense advantages offered by pulmonary route and have attracted significant advancements in the pharmaceutical field. However, pulmonary drug delivery has been challenging because of the complexity of the respiratory tract and the existing defense mechanism. The pulmonary drug delivery has experienced advances in approaches and strategies to combat the existing challenges by tailoring the physicochemical properties of the delivery carriers and enabling both localized as well as systemic delivery. Pulmonary drug delivery is governed by several biophysical parameters of the delivery carriers such as particle size, shape, density, charge, and surface modifications. Although much attention has been garnered for other parameters particle shape effects have been less likely explored. In this exploration we studied the impact of particle shape on the aerodynamic properties, ability to escape macrophage uptake and therapeutic effectiveness of particles against lung cancer. Interestingly, the results of in-vitro lung deposition demonstrated improved aerodynamic properties of the rod-shaped with high aspect ratio as compared to spherical particles. Results of macrophage uptake demonstrate that high aspect ratio particles were internalized less when compared to spherical particles. On the contrary, results of cellular uptake by small cell lung cancer cells revealed preferential uptake of rod-shaped particles than spherical particles. The results were further validated by in-vitro tumor simulation studies

المنارة للاستشارات

www.manaraa.com

wherein rod-shaped particles displayed enhanced anti-tumorigenic activity against spheres. Moreover, the high aspect ratio particles also demonstrated diminished cardiotoxicity activity; adverse effect of DOX limiting its therapeutic use. These results provide valuable insights about influence of particle shape for designing inhalable therapeutics.

www.manaraa.com

ACKNOWLEDGEMENTS

Though thesis is an individual work, I could never have reached the heights or explored the depths without the help, support, guidance, and efforts of a lot of people. It is a pleasant task to express my thanks to all those who contributed in many ways to the success of this study and made it an unforgettable experience for me.

Firstly, I would like to thank my mentor Dr. Vivek Gupta for instilling in me the qualities of being a good researcher. This feat was possible only because of the unconditional support, the infectious enthusiasm and unlimited zeal from Dr. Gupta which served as the major driving forces through my post-graduate career. I would also like to acknowledge to my committee members; Dr. Abu Serajuddin, Dr. Sandra Reznik, Dr. Aaron Muth, Dr. Nitesh Kunda and Dr. Sunny Guin for their suggestions and comments during my dissertation journey.

I thank Dr. Vijaya Korlipara for serving as the serving as the chair of my dissertation committee and the Department of Pharmaceutical Sciences for providing me with all the necessary support needed. I am deeply grateful to the College of Pharmacy and Health Sciences and the Dean's Office for providing me financial support and facilities to carry out my research

I am indebted to my many friends for providing a stimulating and fun filled environment. My thanks goes to my lab mates; Nishant, Abdul, Vineela, Lucy, Gautam, Sruthi and Mimansa who have been very supportive to make this journey smooth and memorable.

www.manaraa.com

Words fail me to express my appreciation to my Mom and Dad for their support, generous care, sincere encouragement, and inspiration throughout my research work and lifting me uphill this phase of life. My very special thanks to the one person whom I owe everything I am today, my father, Krishnakumar Shukla. His unwavering faith and confidence in my abilities and in me is what has shaped me to be the person I am today. I would also like to extend huge, warm thanks to my brother who besides his busy schedule never failed to help and motivate me.

www.manaraa.com

TABLE OF CONTENTS

www.manaraa.com

www.manaraa.com

LIST OF TABLES

www.manaraa.com

LIST OF FIGURES

www.manaraa.com

www.manaraa.com

www.manaraa.com

1.0 Introduction

Respiratory diseases are defined as pathological condition which affect the respiratory airways and other structure of lungs impacting their function [1]. They can be classified based on the severity of disease as; 1) mild and self-limiting: common cold and 2) chronic and life-threatening: asthma, chronic obstructive pulmonary disease (COPD), lung cancer etc. As per WHO (World Health Organization) report, respiratory diseases account for ~30% deaths occurring worldwide [2]. The global burden of mortality due to respiratory diseases has been contributed significantly by lower respiratory infections, lung cancer and COPD accounting ~16.2 million deaths [2]. Pulmonary drug delivery has been serving as first-line treatment for several respiratory diseases since the 20^{th} century. Characterized by large surface area (~100 m^2 in adult humans), extensive blood capillary network, very thin absorptive mucosal membrane and air-blood interface facilitating increased permeation, enhanced absorption and improved pharmacokinetics of inhaled therapeutics, pulmonary delivery offers diverse advantages [3,4]. Significance of pulmonary delivery also involves features such as overcoming first pass metabolism, limited degradation of therapeutics , reduced side effects, increased localized concentration and enhanced therapeutic effect with only a fraction of dose [5,6]. For example, salbutamol when given orally requires an oral dose of 2 mg to 4 mg while only 0.1mg-0.2 mg dose is required upon inhalation to provide the same therapeutic effect [7]. Similarly, in a comparative clinical study performed in healthy men, difference in pharmacokinetics of oral vs. inhaled terbutaline was observed wherein inhalation of drug resulted into ~3 folds increase in bioavailability of the drug as compared to oral administration [8].

www.manaraa.com

Local delivery to lungs have been widely explored for treatment of pulmonary diseases and advances has been made over decades to develop efficient lung delivery systems. Development of modern inhalation devices such as nebulizers, dry powder inhalers and metered dose inhalers have improved the delivery of therapeutics to lungs. Commercially available inhalation products for such as Advair® (Fluticasone and Salmeterol), Symbicort® (Budesonide and Formoterol), Triohale® (Ciclesonide, Formoterol and Tiotropium), TOBI® (Tobramycin), Colobreathe® (Colistimethate) have perceived the success of pulmonary drug delivery for treatment of asthma, COPD, and bacterial infections [9]. Recent FDA approval of Arikayce® inhalation suspension comprising of amikacin encapsulated liposomes have paved the path for amalgamation of nanotechnology with traditional pulmonary delivery methods [10]. Despite these advancements, pulmonary delivery systems suffers several limitations such as short half-life, rapid elimination and low dose deposition impacting bioavailability followed by frequent dose administration thereby passively impacting patient compliance [11,12]. To address these issues, it is essential to understand the anatomical challenges existing and tailor the biophysical parameters accordingly to design inhalable carriers which could lead to development of optimized efficient carrier systems.

1.2 Physiological structure of the respiratory tract- A brief overview

The anatomical structure of human respiratory tract influences the flow passage of air subsequently impacting the orientation and deposition of inhaled particles. The respiratory tract is divided into two parts: 1) the upper respiratory tract consisting of nose, nasal cavity and pharynx which is responsible for transporting air from external environment to the sites of gas exchange and 2) the lower respiratory tract comprising of

www.manaraa.com

larynx, tracheobronchial region and alveolar region which are involved in gas exchange [13]. Pulmonary airway structure originates from the oro-pharynx region followed by larynx and trachea. The trachea is fused with the larynx and enters in each side of lungs as primary bronchi which divides into bronchioles paving the pathway for the air to reach the respirable region in lungs [14]. The bronchioles branch into primary bronchioles, secondary bronchioles, and respiratory bronchioles. Respiratory bronchioles terminate into alveolar region comprising of alveolar ducts and alveolar sac [15]. The bronchi and bronchioles are responsible for conducting the air to the alveolar region where the gas exchange takes place. About 480 million alveoli are present in an adult lung and each alveolus is lined with extensive pulmonary capillary resulting into huge surface area of 70-140 m^2 being available at the air-blood barrier for the exchange to take place [16,17].

In terms of cellular composition, respiratory tract is formed by continuous layer of epithelial cells which are designed to perform specific functions such as: providing barrier for protection against harmful agents, muco-ciliary clearance, secrete protective substances to destroy the external agents and modulate immunogenic responses [18]. The epithelium layer of the respiratory tract is shown to be possess about 40 different cells for accomplishing successful respiration, indicating the complexity and heterogeneity as it progresses from the trachea to the alveolar region as seen in **Figure 1** [14,19]. The airway epithelium in the conducting airways (trachea and bronchi) is pseudostratified and columnar comprising of goblet cells (secreting mucus), basal cells and ciliated cells (causing muco-ciliary escalation). The apical membrane of the cells have tight junctions thereby providing a tight physical barrier for the entry of pathogen [20]. The conducting airways epithelial region is also covered with pulmonary mucous lining. This mucus barrier

www.manaraa.com

is composed of two different layers: the top layer is viscous gel like comprising of several macromolecules having capacity to entrap wide range of inhaled particulates and is continuously cleared by ciliary beating [21]. Mucus is comprised of water (95–97%), mucin (glycoprotein), immunoglobulins, albumin, lysozyme, and lactoferrin [22]. While the bottom layer is the periciliary layer which is a thin watery-sol layer composed of minimal glycoproteins and proteins. The periciliary layer prevents mucus penetration in the periciliary space and help in facilitating the ciliary activity [23]. In adults, the mucus layer is reported to be renewed every 20 minutes and the mucus clearance rate is recorded to be 3–25 mm/min [24]. Farther down the respiratory airways in the bronchiole region, epithelial layer consist of simple columnar cells having shorter cilia which are more like cuboidal shape and secretory club cells also known as Clara cells (**Figure. 1)** [14,20]. Moreover, the thickness of mucus lining which is ~ 10–30 μm in the tracheal region also decrease progressively in the distal bronchioles to 2–5 μm [24].

The alveolar region has very a thin epithelial layer which is comprised of two types of pneumonocytes: alveolar type I (AT-I) and alveolar type II (AT-II) cells. AT-I cells are large, flat squamous cells covering ~90% of the alveolar surface and are responsible for gas exchange due to their thin gas permeable membrane [20,25]. AT-II cells are small cuboidal cells responsible for secretion of surfactants which lines the alveolar epithelium providing the air-liquid interface [26]. The presence of surfactants help in reducing the surface tension and thereby prevent the collapse of alveolar surface [27]. Pulmonary surfactant comprises of a complex mixture of 92% lipids and 8% surfactant proteins (SP) [28]. Amongst, the surfactant proteins SP-A and SP-D are large hydrophilic SPs also known to induce immunomodulatory response by binding to the invading pathogen,

www.manaraa.com

causing opsonization and further inducing phagocytosis [28,29]. While SP-B and SP-C are the hydrophobic SPs responsible for maintaining the surfactant adsorption dynamics [30]. Resident alveolar macrophages present in the interstitial space are responsible for engulfing any pathogen or debris of inhaled particulate [31].

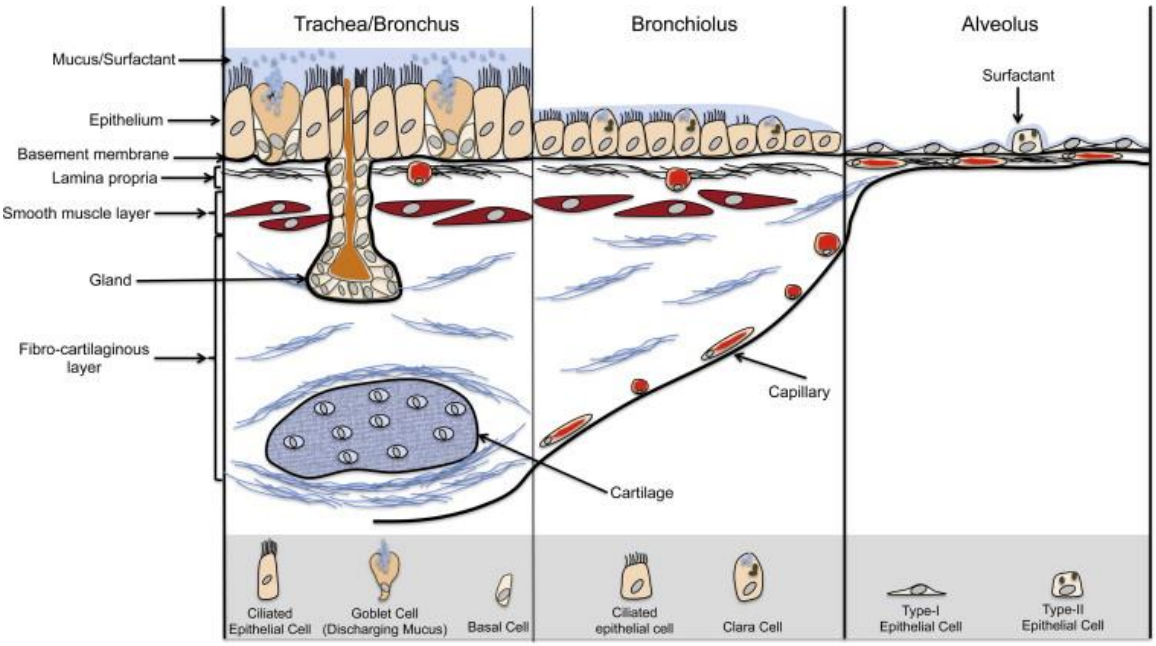

Figure 1: Schematic representation of cells present in different regions of the respiratory structure [14].

1.3 Understanding the Fate of particles upon entry into the respiratory tract

As can be seen in **Figure 2** after inhalation, the particles first enters the central lungs wherein they interact with the mucociliary layer. Depending on the physicochemical properties the particles may either permeate the layer and reach the epithelia or may get cleared from lungs via mucociliary clearance [32]. If the particles do not deposit and successfully evade clearance in the central lung, they reach the peripheral lung (**Figure 2**). The biophysical parameters of the particles may then determine the deposition of particles in the conducting airways and its successful absorption [17]. The inhaled particles may get

www.manaraa.com

internalized by alveolar macrophages depending on the particle properties which will be discussed in detail in the following sections.

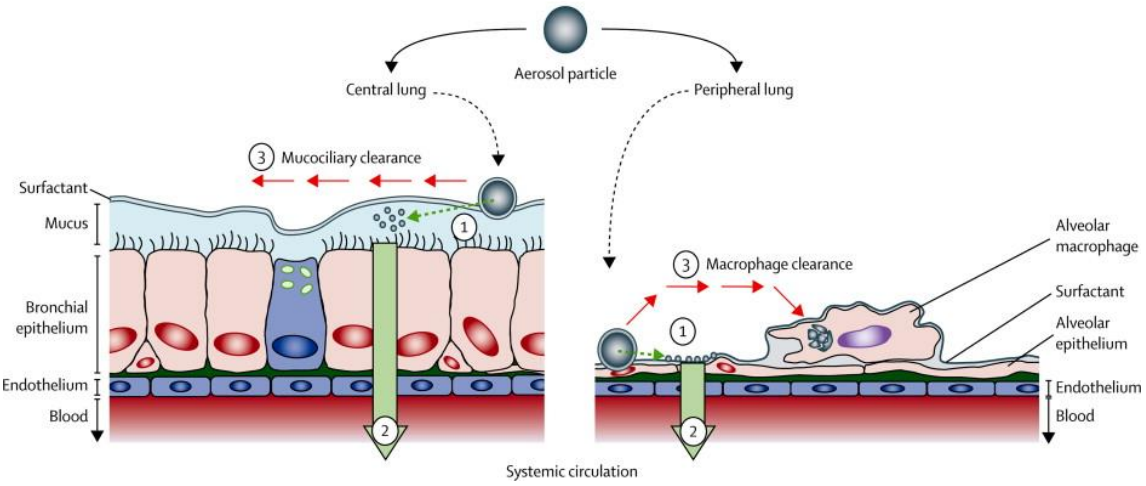

Figure 2: Fate of particles upon entering lung. The figure represents following steps 1) deposition of particles on the airway epithelia 2) absorption/translocation of particle from epithelia to blood circulation and 3) clearance by existing pulmonary barriers [26].

1.3.1 Step 1: Deposition of particles in respiratory tract

Upon entering the respiratory tract, inhaled particles are carried further in the respiratory airways by the tidal air and mechanical forces such as gravity, inertia and impulse collision along with the gas molecules resulting into deviation of their trajectories from the streamlines causing them to deposit at varied site [33]. Inhaled particles in lungs tend to deposit in the lungs based on following deposition mechanisms governed by their physicochemical properties:

Inertial impaction: Larger particle (>5 μm) tend to deposit via inertial impaction wherein the particles are incapable of streamlining themselves and deviate from the flow each time when there is a bifurcation or change in the flow direction [34]. This deposition pattern is observed in upper airways where the particles deviating from their trajectories impact the site of deposition due to sudden change in the direction of air flow [35].

www.manaraa.com

Gravitational sedimentation: Gravitational sedimentation refers to settling of particles under the influence of gravity and is observed by particle within 1 to 8 μm range [33]. This deposition mechanism has direct relationship with the particle size and residence time of particles in the airways [35]. Gravitational sedimentation is commonly observed in smaller airways and alveolar region where the residence time is high and the particles have less distance to cover before reaching the airway walls [36].

Diffusion (Brownian motion): Diffusion is observed by particles of <0.5 μm which are deposited into alveolar region by this deposition patter due to low air velocity in the region [37]. Brownian motion of the particles occur upon collision with gas molecules resulting into random motion of the particles [36]. This pattern of deposition has inverse relationship with particle size where smaller the particle, higher is this deposition pattern observed [35,38].

Interception: This deposition mechanism is observed for particle that are fiber-like, elongated and have high length to width ratio (also known as aspect ratio). An increase in elongation of particle results into increase in probability of deposition by this mechanism [33,36,38]

Inhaled particles are deposited in different regions of the lung based on their size, shape, density, charge, and surface properties of the particles. After deposition, the aerosol particulates must overcome the existing pulmonary barriers to reach their targeted site. The respiratory system eliminates the inhaled particles using pulmonary barriers depending on the site of deposition (**Figure. 2)**.

www.manaraa.com

1.3.2 Step 2: Drug dissolution and absorption in the lungs- Translocation of particles

After deposition of particle on the respiratory surface, the particle must dissolve or permeate the epithelia (bronchial or alveolar) for absorption [32]. Hydrophilic molecules are rapidly absorbed and translocated to the systemic circulation; however, large hydrophilic protein molecules post-deposition can interact with pulmonary surfactants resulting into aggregation of particles hindering their absorption and eventually being phagocytosed by alveolar macrophages [12]. On the contrary studies have reported that lipophilic particles after deposition encounters with pulmonary surfactant which enhances their permeability, solubility, and bioavailability [39,40]. Similarly, particles surface modification also determines the translocation ability of the deposited particles. Cationic and hydrophilic surfaces are reported to exhibit prolonged absorption and minimal translocation when compared to neutral or negatively charged particles [41]. Choi *et al*., have evaluated the translocation of florescent labeled nanoparticles of varied size ranging from 5 to 300 nm and functionalization after intratracheal administration in Sprague-Dawley (SD) male rats. Results illustrated that nanoparticles of < 36nm particle size translocated from lung to lymph nodes, while extremely (<6 nm) small nanoparticles rapidly translocated to lymph nodes and systemic circulation following which they were cleared by kidneys. They have also demonstrated the impact of surface charge on translocation of particle, wherein cationic charged particles inhibited pulmonary translocation while neutral (polyethylene glycol coating) or zwitterionic (cysteine coating) resulted into prompt translocation to various target organs [42]. Liu *et al*, assessed the *in-vivo* impact of size of radiolabeled particles (20 nm to 5 µm) on translocation from lungs.

www.manaraa.com

Large sized particles (~2 to 5 μm) were cleared by mucociliary clearance and translocated to systemic circulation and other organs such as kidney, liver, spleen, thyroid, and heart. On the other hand, smaller particles were found to have prolonged retention in lung and translocated to blood, liver, and thyroid with reduced clearance [43]. Recently Buckley *et al*., performed inhalation study on rats to evaluate the effect of particle size on clearance and translocation of radioactive labeled iridium loaded nanoparticles ranging from 10 to 75 nm in size. They have reported low levels of particle size dependent translocation of nanoparticles from lungs to organs such as kidney, liver, and brain with maximal deposition occurring in kidney which subsequently is cleared [44]. Therefore, the physicochemical properties of the inhaled particles governs the translocation of particles to the systemic circulation, lymphatic system and or other target organs.

1.3.3 Step 3: Overcoming pulmonary barriers impacting the deposition of aerosol in lungs.

A) Mucociliary clearance

Mucociliary clearance is the first line of defense mechanism offered in the conducting airways. The principal of mucociliary clearance involves entrapment of inhaled particulates in the thick mucus layer and escalating it by the ciliary beating towards larynx or pharynx where they are either swallowed or coughed [45]. After deposition of particles in the tracheobronchial region, the particles encounter with thin luminal surfactant lining resulting into displacement of particle from the air interface to the underneath mucus layer [46]. As the mucus layer is continuously moving proximally, the entrapped particles are cleared immediately by either coughing or swallowing [3]. If the particles successfully escape the mucociliary escalation, pulmonary dissolution of drug in the epithelial lining is

www.manaraa.com

required for effective absorption of the inhaled drug. Hydrophilic drug molecules which are freely soluble are rapidly absorbed while hydrophobic molecules are retained longer and is highly susceptible to respiratory clearance [5]. Mucociliary clearance rate is known to be increased with the increase in thickness of the mucus layer and the diameter of the airways . Therefore, particles depositing in the proximal conducting airways are escalated faster towards the larynx/pharynx resulting into their clearance [5]. Stahlhofen *et al*., has demonstrated that particles larger than 6μm are easily entrapped in the mucus layer and are subjected to mucociliary clearance while smaller particle are retained comparatively for longer time [47,48]. However, Smith *et al*, demonstrated that particle size difference does not impact the airway clearance of gold particles (d_p 1.2 μm) and polystyrene (d_p 5 μm) administered using bonus inhalation and that both the particles displayed similar retention in the lungs [49]. Furthermore, studies performed by Henning *et al.* revealed no significant difference in the mucociliary clearance of particles evaluated for size ranging from 50 nm to 6000 nm. On the contrary, material properties and surface chemistry of the particles were found to impact the mucociliary clearance [50]. Mucociliary clearance serves as an important defense mechanism against the invading agents, however, in some disease conditions its function is impaired which affects the retention and efficacy of the inhaled drugs [51]. Therefore, designing delivery carriers to impart prolonged residence and improved therapeutic activity by tailoring their properties can be a promising strategy.

www.manaraa.com

B) Clearance by Alveolar Macrophages

Alveolar macrophages are present in the interstitial space in the alveolar region and are recognized as the first line of cellular host defense [52]. Macrophages are phagocytic cells which secret various cytokines or chemokines to activate the immune system against the invading pathogen or particulate matter [53]. Alveolar macrophages display non-absorptive clearance mechanism. These macrophages adhere to the inhaled particle by either receptor binding or electrostatic interaction and engulf them. The engulfment can be mediated by surface cavitation, vacuole formation or pseudopod formation [54].

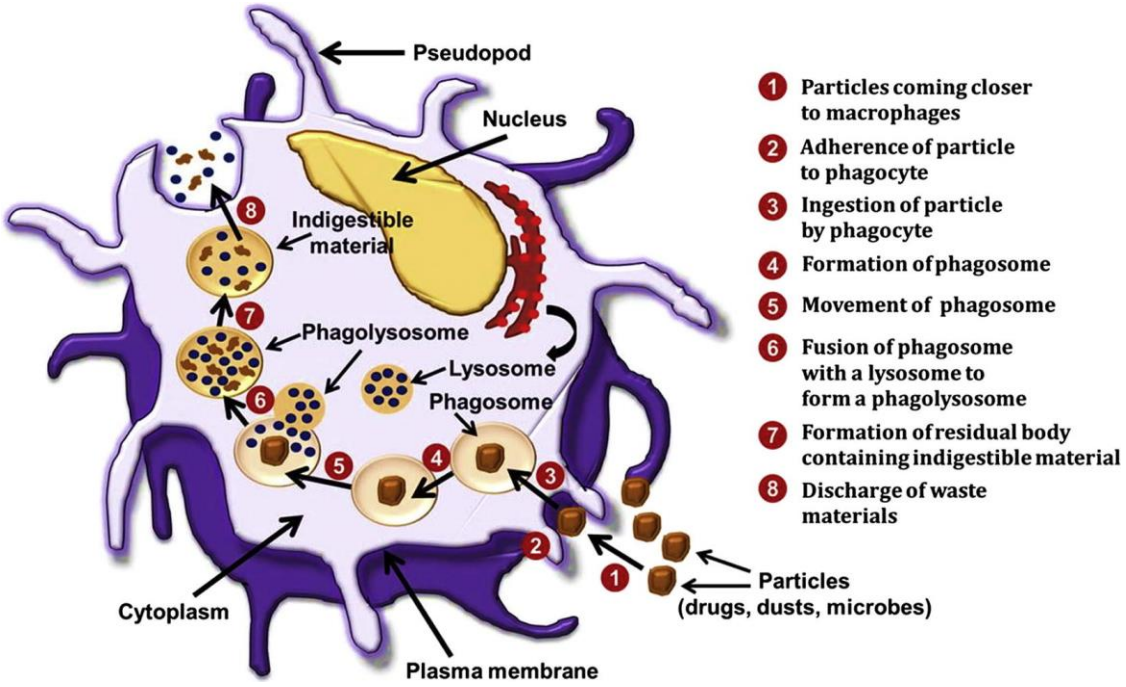

Figure 3: Schematic representing the process of phagocytosis of particles by macrophages [55]**.**

www.manaraa.com

Figure 3 represents detailed phagocytosis process of macrophage. As can be seen the first step of phagocytosis involves particles being present in the vicinity of macrophages followed by attachment of the particle to the surface of macrophages. Upon attachment of particle, pseudopod (cup-like structure) formation occurs via actin remodeling for engulfment of the particles. After successful engulfment of particle, phagosome formation occurs which later fuses with lysosome to form phagolysosome (**Figure 3)**. The phagolysosome degrades the particles by enzymatic action or acidic environment and discharge the waste in the lymphatic system [55].

C) Clearance by Enzyme Degradation

Inhaled particles are also susceptible to degradation in lungs due to the presence of several enzyme. Several enzymes are present in lung to maintain its physiological function and serve as defense mechanism against the inhaled particles and xenobiotics along with preserving the homeostasis [56]. Although, lung has relatively low level of enzyme activity compared to liver, it is more comparatively more inducible [57]. Predominantly enzymes belonging to cytochrome (CYP) P450 family such as flavin-containing monooxygenases (FMO), monoamine oxidase (MAO), aldehyde dehyrogenase, NADPH-CYP450 reductase is found throughout lungs [39]. Carboxylesterases responsible for hydrolysis of diverse functional groups such as esters, amides, thiols and fatty acids are found to expressed in human lungs [58]. Esterase, liable for cleavage of ester bonds are found extensively in alveolar macrophage and in minimal amount in alveolar type I and II cells [4]. Proteases responsible for degradation of proteins and peptides are present on the surface of bronchial and alveolar epithelial cells [59].

www.manaraa.com

1.4 Essentials for Successful Pulmonary Delivery

For efficient delivery to lungs, inhaled delivery carriers must reach the desired site of action which in most respiratory disease is peripheral lungs, and evade phagocytic uptake by alveolar macrophages [1,19]. Advances in the field of pulmonary drug delivery have identified several tunable bio-physical parameters that influences the drug delivery to the lungs. Parameters such as particle size[4–6], density[7–9], rigidity[10,11], hygroscopicity[12–14] and surface chemistry[15–17] have been reported to govern the fate and deposition of particles in lungs.

Despite the advancements, dug delivery to lungs suffers limitations such as low dose deposition, rapid elimination of inhaled particles by existing defense mechanisms, short half-life, impacting bioavailability and patient compliance [7,18]. The importance of particle shape was illuminated after understanding the enhanced and prolonged retention of respiratory disease-causing microorganisms such as Mycobacterium tuberculosis, Hemophilus influenza, Legionella pneumophila and Pseudomonas aeruginosa in lungs [20–22]. While inhaled particulate delivery carriers are known to be rapidly eliminated from lungs, these microorganisms on the other hand demonstrate prolonged retention in the peripheral lungs after overcoming the existing lung defense mechanisms, thus causing severe to cause various respiratory diseases. It is interesting to comprehend that the shape of these micro-organisms causing respiratory diseases in peripheral lung are known to be aspherical or rod rod-like, shapes which is suggestive to play an important role in enhancing their aerodynamic properties[23], and evading clearance by lungs' defense mechanisms [23,24].

www.manaraa.com

In addition to aspherical Additionally, microorganisms, rod-shaped, or fibrous particles such as asbestos and carbon nanotubes are deposited in the alveolar region and result into adverse health effects implying that particle shape enhances aerodynamic behavior of particles [25,26]. Several computational fluid dynamic (CFD) studies have revealed the deposition performance of fibers or elongated particles in lungs wherein they are reported to orient themselves parallel to airflow and hence travel preferentially to the distal region of lungs [27–29]. However, experimental respiratory deposition data or in-vitro deposition behavior of such anisometric rod-shaped or fibrous particles has not been thoroughly examined [30], . Thereby indicating the dire need to experimentally investigate the role of particle shape further experimentally on aerodynamic behavior and peripheral lung deposition of aspherical particles in lungs.

Along with particle deposition, cellular internalization is another paramount factor deciding the therapeutic fate of particles in lungs. Several studies have highlighted the details of particle shape and its role in phagocytic uptake wherein rod-shape or filamentous particle being successful in evading the uptake by macrophage [31–33]. It has been shown that not only the shape of particle but also the orientation of particle or target geometry encountering the surface of cells determines their internalization of into target cells [31,34]. Target geometry of particles is defined by the contact angle wherein particles with high curvature regions are known to escape the uptake by macrophages [32,34]. On the other hand, studies have reported that non-spherical particles are readily internalized by various cancer cells as compared to their counterparts [33,35,36]. In a recent study, by He and Park, examined the influence of 20 different shapes and sized particles on the internalization by cancer cells. Their results have reported that local interaction between

www.manaraa.com

particle and cell surface determined the internalization fate of particles, and elongated particles with sharper angular features were readily internalized [36]. Thus, fine fine-tuning the particle shape of inhaled delivery carriers may serve as a potential strategy to address the existing limitations of pulmonary drug delivery systems and improving their therapeutic efficiency.

The aim of the present study is to explore novel strategy of particle shape fabrication modulation for development of effective inhaled delivery carriers possessing peripheral lung deposition with efficient aerodynamic properties and capability to evading macrophagic uptake. We have utilized Doxorubicin hydrochloride (DOX) as a model drug to evaluate the influence of particle shape on the therapeutic effectiveness of the delivery carriers. The aerodynamic properties of the varied size and shaped particles was evaluated using in-vitro lung deposition simulator, next generator impactor (NGI). Further, therapeutic activity of various DOX-conjugated particles was assessed by systematic in-vitro studies performed on small cell lung cancer chosen as a model pulmonary disease. Additionally, as DOX is known to be limited for its therapeutic use because of cardiotoxicity, the influence of particle shape in overcoming this limitation of DOX was also examined.

www.manaraa.com

2.0 Hypothesis

"Particle shape modification enables significant deep lung deposition with efficient aerodynamic properties".

To test this hypothesis, the following questions will be addressed in this exploration:

1.) Could the particles with varied shape be fabricated?

2.) Does particle shape influence the aerodynamic behavior?

3.) Does particle shape impact the uptake by macrophages?

4.) Could particle shape improve the efficacy of drug against lung cancer?

5.) Could particle shape reduce the toxicity of drug?

www.manaraa.com

3.0 Materials and Methods

3.1 Materials

Polystyrene microspheres of different sizes (0.5 µm, , 6.0 µm and 10µm) were purchased from PolySciences, Inc. (Warrington, PA, USA). Poly (vinyl alcohol) (PVA-fully hydrolyzed) was obtained from Sigma Aldrich (St. Louis, MO, USA). Doxorubicin hydrochloride (DOX) was procured from LC laboratories (Woburn, MA, USA). Phosphate Buffer saline (PBS) pH 7.5, dimethyl sulfoxide (DMSO) and HPLC grade solvents such as acetonitrile and water were purchased from Fisher Scientific (Hampton, NH, USA). Various other assay kits and other molecular biology grade reagents were obtained from several sources which have been listed along with their respective methods.

3.2 Cell Culture

Murine macrophages RAW 264.7 cells, multidrug resistant human small cell lung cancer (SCLC) cell line H69AR and rat cardiomyoblasts H9c2 cells were acquired from American Type Culture Collection (ATCC) (Manassas, VA, USA). H69AR cells were cultured in Roswell Park Memorial Institute (RPMI) 1640, while RAW 264.7 and H9c2 cells were grown in Dulbecco's Modified Eagle's Medium (DMEM) (Corning Inc., Corning, NY, USA), supplemented with 10% fetal bovine serum (Atlanta Biologicals, Flowery Branch, GA, USA), 1% sodium pyruvate and 1% penicillin-streptomycin (Corning Inc., Corning, NY, USA) by incubation at 37°C under 5% CO_2. 3-(4,5-dimethylthiazol-2-yl)-2,5-diphenyltetrazolium bromide (MTT) and crystal violet were obtained from Fisher Scientific (Hampton, NH, USA). Vectashield hardset mounting medium kit with DAPI was procured from Vector Laboratories Inc. (Burlingame, CA, USA).

www.manaraa.com

3.3 Particle Fabrication

Spherical particles were fabricated to rod-shaped particles using one dimension stretching method as reported earlier with slight modifications [9]. As can be seen in **Figure 1A,** carboxylated functionalized polystyrene particles of different sizes (0.5 µm, 6.0 µm and 10µm) were dispersed in poly-vinyl alcohol (PVA) film; and were subsequently stretched to desired length in an oil bath using custom made apparatus.

3.3.1 Film preparation

Briefly, 5% PVA (~2 g in 30 ml of water) was dissolved in water at 85°C with continuous stirring. After complete dissolution of PVA, 2% (w/v) glycerol was added as plasticizer to the PVA solution. The resultant mixture was then allowed to cool and spherical polystyrene particles (~0.75 mL) were added to this mixture. The mixture was later carefully poured on a 13 × 13-cm petri plate to avoid entrapment of any air bubble in the film. Resultant films were dried completely for ~48 hrs, and stored in a dry place until further use.

3.3.2 Film stretching

The dried film was cut into sections of ~5 × 5 cm and mounted on the custom-made stretchers [60,61]. The stretcher comprised of two aluminum blocks mounted on a screw. After mounting the film on the blocks, the length of the film in between the two blocks was measured which helped in determining the final distance for separation. The stretcher along with the mounted film was immersed in hot mineral oil (~120°C) for 5 min and stretching was performed by keeping the stretcher in the oil bath (**Figure 4)**. Stretching of the film was performed to 3 folds or 6 folds of the initial length of film mounted between aluminum blocks to obtain rod shaped particles of varied lengths. Short rods (SR) were obtained upon

www.manaraa.com

stretching the films to 3 folds of its initial length while 6 folds stretching resulted into long rods (LR) After stretching to the desired distance, film was cooled for 10 minutes before unmounting from the stretcher.

3.3.3 Particle recovery

The stretched film was removed from the stretcher and cut into extremely small pieces which were dissolved in water at 70°C. The particles were washed by centrifugation at 10,000xg for 10 minutes with water. The washing was performed thrice to remove PVA from the mixture. The recovered stretched particles were finally redispersed in 1 mL of water and stored at 4°C until further use.

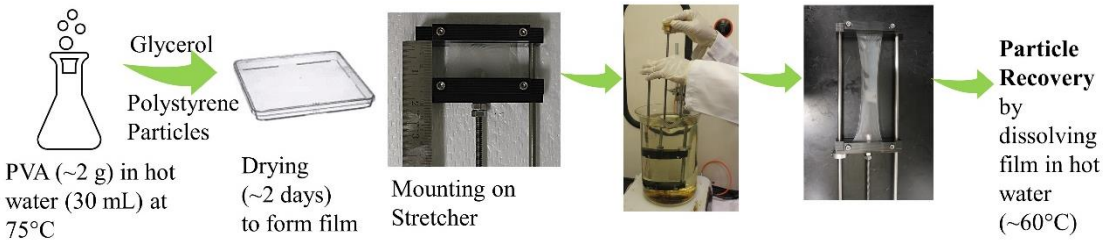

Figure 4: Schematic representation of fabrication of particles of varied shapes using the stretching method.

3.4 Structural Morphology

Morphology of the fabricated particles were examined using Nova Nano SEM™ 450 and Helios Nano Lab 660 (FEI, Hillsboro, Oregon, USA). Briefly, the particles were dried on the SEM pin stub (Ted Pella, Inc., Redding, CA, USA) and then sputter coated with palladium for 90s and imaged at 5 kV. The dimensions of particles were obtained by measured 30 particles (n=3) from each of the obtained micrographs using Image J analysis software.

www.manaraa.com

3.5 Conjugation DOX on Spherical and Stretched Particles

Conventional carbodiimide chemistry was used for conjugating carboxylate groups on particles' surface to the amine group of DOX resulting into formation of amide bond as shown in **Figure 5**. Briefly, 1mg of particles were added to aqueous solution containing excess 1-Ethyl-3-(3-dimethylaminopropyl) carbodiimide (EDC) and N-hydroxy succinimide (NHS) and stirred for 3 hrs. at room temperature. This reaction allowed the carboxylic groups to be activated. Particles were then centrifuged to remove the excess of EDC and NHS followed by washing to ensure complete removal of the reagents. The activated particles were then incubated with excess amount of DOX (1 mg) for 72 hrs. Following incubation period, the unconjugated drug was separated by centrifugation at 10,000xg for 10 minutes and further washing particles twice with water. Additionally, the conjugated particles were finally washed with methanol to remove any free DOX. The DOX-conjugated particles were finally resuspended in water and stored at 4°C for further analysis. Spheres of all size used for conjugation were also recovered from the film after placing them in the hot oil bath as mentioned in section 3.3. This was done to expose the carboxylic groups of spheres to the conditions like that of SR and LR.

The amount of drug conjugated was determined by measuring the absorbance at 485nm using TECAN plate reader (Tecan Group Ltd., Männedorf, Switzerland).

www.manaraa.com

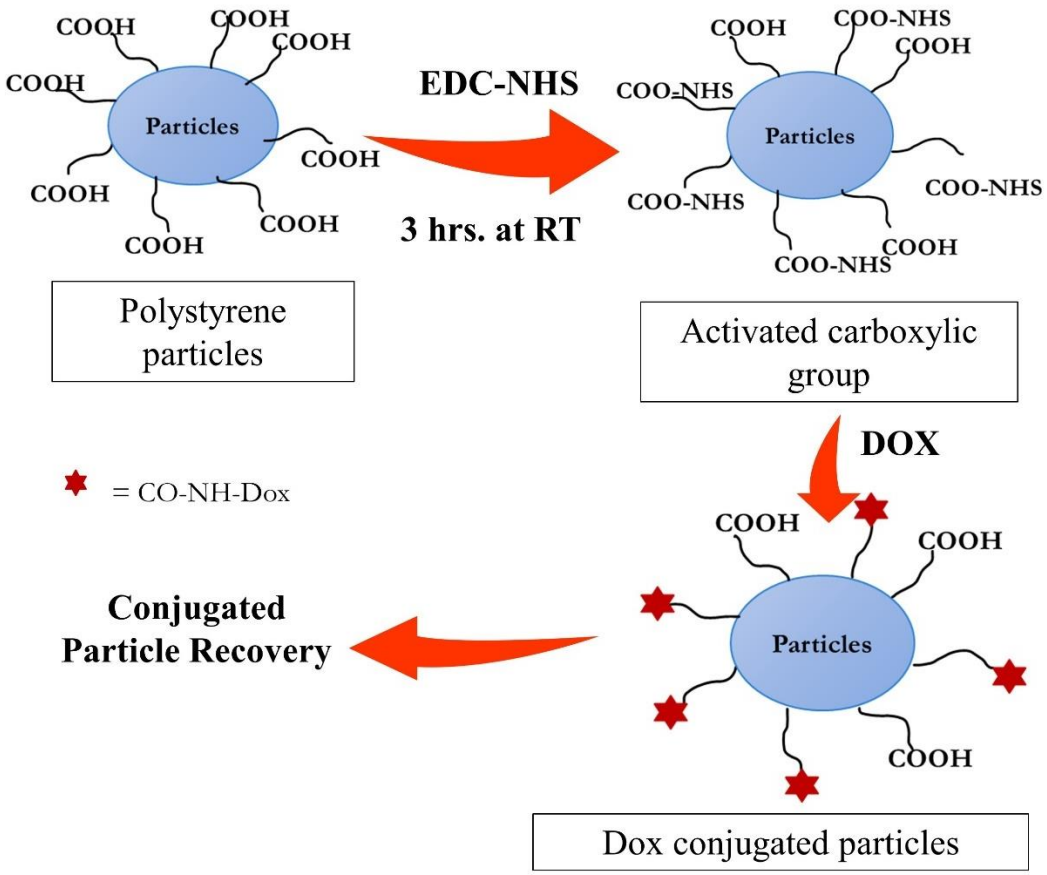

Figure 5: Reaction scheme for conjugation of DOX to the carboxylic groups present on the surface of the polystyrene particles using EDC-NHS chemistry.

3.6 Characterization of DOX Conjugation

3.6.1 DSC studies

Calorimetric studies of DOX, blank 10µm particles, physical mixture of DOX and blank particles and DOX-conjugated particles were performed using DSC 6000 (Perkin-Elmer; Waltham, MA, USA) equipped with an intra-cooler accessory. About 1.5 mg of sample was sealed in an aluminum pan, while a sealed empty pan was maintained as reference. The samples were analyzed over the temperature range of 50°C to 300°C at a heating rate of 10°C/min maintained under a nitrogen purge having flow rate of 50 mL/min.

www.manaraa.com

3.6.2 FT-IR

FT-IR analysis of the samples were performed using a Spectrum-100 (Perkin-Elmer, Inc.; Shelton, CT, USA) equipped with attenuated transmittance reflectance (ATR). The spectra of DOX, blank particles, DOX-conjugated particles, and physical mixture of DOX and blank particles were measured for comparison over 1000-4000 cm^{-1} range.

3.7 *In-vitro* Pulmonary Deposition Behavior

In-vitro deposition behavior reflects the aerodynamic behavior of the inhaled particles and can be used to estimate the deposition pattern of particles *in-vivo* [62]. *In-vitro* deposition behavior of DOX-conjugated particles were assessed using Next Generation Impactor (NGI, MSP corporation, MN, USA) to predict the impact of particle shape on aerodynamic properties using previously reported method [63,64]. Briefly, 2 mL of DOX-conjugated particles at concentration of 450 µg/mL were nebulized using jet nebulizer, PARI LC PLUS® nebulizer cup connected with Pari FAST-NEB compressor system into pre-cooled impactor under vacuum maintained at 15 liters/minute for 4 minutes. The NGI was previously cooled at 4°C for 90 minutes to avoid heat-transfer which otherwise may cause shrinkage of the nebulized droplets, thus causing impact on particles' deposition behavior [65]. Following nebulization, particles deposited on each stage of NGI were collected using a cell scrapper and were analyzed for drug amount present using TECAN plate reader (Tecan Group Ltd., Männedorf, Switzerland), as described earlier. Aerodynamic parameters such as fine particle fraction (% FPF) and mass median aerodynamic diameter (MMAD) were calculated from the amount of drug deposited in each stage. % FPF was determined as the fraction of emitted dose deposited in the NGI

www.manaraa.com

stages with <5.39 μm while MMAD (d_{ae}<5.39 μm) representing the aerodynamic particle size distribution was calculated using log-probability analysis (n=3) [64].

All the further experiments were performed using10μm DOX-conjugated particles (spheres, short rods, long rods).

3.8 *In-vitro* Release Studies

In-vitro release studies of all 10μm DOX-conjugated particles (spheres, short rods, long rods) were performed using release method as previously reported with slight modifications [66]. Briefly, 2 mg of DOX-conjugated particles were dispersed in 5 mL of PBS pH 7.4 and acetate buffer pH 5.5. The samples were incubated at 37°C with continuous shaking at 50 rpm. At predetermined intervals, the samples were centrifuged at 10,000×g for 10 minutes, and obtained supernatants were analyzed at 485 nm wavelength using TECAN plate reader to determine the amount of DOX released.

3.9 Stability Studies

Stability studies of 10μm DOX-conjugated particles were performed by storing the samples at two different conditions: 4°C (representing normal refrigerated storage) and 40°C/75%RH (accelerated stability storage) for a time interval of 15 days. Following the storage period, the samples were analyzed in terms of particle size along with aspect ratio, change in particle shape and amount of DOX-conjugated as μg of DOX/mg of particles.

3.10 Cellular Uptake Studies

The uptake of different shaped DOX-conjugated particles and free DOX was evaluated on RAW 264.7 murine macrophages and H69AR human SCLC cells using previously reported method [67]. Briefly, 1.0×10^4 cells/chamber were seeded on 8-

www.manaraa.com

chambered imaging coverslip (Eppendorf, Hauppauge, NY, USA) and were incubated overnight at 37°C and 5% CO_2. Cells were treated with DOX-conjugated particles or free DOX (2.9 µg/mL) for 3 hours, following which they were washed twice with ice-cold PBS (1X). The cells were then fixed using 4% paraformaldehyde for 10 mins and then again washed with PBS (1X) to remove excess paraformaldehyde. The coverslip was separated from chamber and was mounted on a clear glass microscopic slide using VECTASHEILD hardset mountant containing DAPI (H1500, Vector laboratories). The cells were then imaged using EVOS-FL fluorescence microscope (Thermo Fisher Scientific, Waltham, MA, USA) at 20X magnification.

In addition to qualitative assessment, intracellular quantification of DOX was also performed for understanding cellular uptake according to previously published method [67]. Briefly, RAW 264.7 macrophages and H69AR cells were seeded at a density of 1.0 x 10^6 cells/well in 6-well plates and incubated overnight at 37°C and 5% CO_2. The cells were then treated with DOX and DOX-conjugated 10µm particles for 1 hr. and 3 hrs. After the respective time interval, the treatment was aspirated, and cells were washed twice with ice-cold PBS (1X). The cells were scrapped using cell scrapper and centrifuged to obtain a cell pellet. The obtained pellet was washed twice using 1X PBS and was lysed using 100 µL DMSO. The lysed pellet was centrifuged again, and the obtained supernatant was subjected to fluorometric analysis. The florescence intensity of DOX in each treatment group was determined at excitation wavelength of 480 nm and emission wavelength of 590 nm using TECAN plate reader (Tecan Group Ltd., Männedorf, Switzerland) [68].

www.manaraa.com

3.11 Cytotoxicity Assessment

The cytotoxicity studies of free DOX and DOX-conjugated 10µm particles were performed on RAW 264.7 macrophages, H69AR DOX- resistant SCLC cells and H9c2 rat cardiomyoblasts using MTT assay. Briefly, RAW 264.7 and H69AR cells were seeded at a density of 2.5×10^3 cells/well while H9c2 cells were seeded at 1.5×10^3 cells/well in tissue culture treated 96 well plates (Eppendorf, Hauppauge, NY, USA), and were incubated overnight at 37°C/5% CO_2. Next morning, cells were treated with different DOX-conjugated particles or free DOX; and were incubated for specific time points; RAW 264.7 macrophages (24 hrs. and 48 hrs.), H69AR cells (72 hrs.) and H9c2 cells (24 hrs.). After respective treatment period, media was removed and MTT (1 mg/mL) was added followed by 2 hrs. of incubation. Later, DMSO was added to each well after aspirating MTT solution. Addition of DMSO helps to dissolve the formazan crystals formed during incubation of cells with MTT solution. The plates were then shaken for 30 minutes on plate shaker and the optical absorption was measured at 570 nm using TECAN plate reader (Tecan Group Ltd., Männedorf, Switzerland). Cytotoxicity of particles was determined by comparing the cell viability against the non-treated cells used as control groups. IC_{50} values were determined by normalizing and transforming the data to log value using Graph Pad Prism Software Version 6.0.

3.12 *In-vitro* Tumor Simulation Studies

In-vitro tumor simulation studies were performed to understand the therapeutic effect of DOX and DOX-conjugated particles by mimicking the *in-vivo* tumorigenic conditions. Briefly, H69AR small cell lung cancer (SCLC) cells were seeded at a density of 1.0×10^3 cells/well in a 96-well U bottom ultra-low attachment spheroid plate (Nuclon® Sphera,

www.manaraa.com

Thermo Fisher Scientific, Waltham, MA, USA) and incubated for 3 days at 37°C/5% CO_2. After incubation, cells were treatment in two different regimens: 1) single dose wherein treatment was provided once only i.e., at the start of experiment and 2) multiple doses where treatment provided every three days until the end of experiment (6 days). During the treatment, half of the initial volume of media was replenished to avoid the possibility of tumor aspiration or tumor damage. The tumors were characterized using several means as outlined below to evaluate the anti-tumor activity of treatments.

a. **Optical Imaging** – Tumor spheroids were imaged at pre-determined intervals using LMI-6000 inverted microscope (LAXCO, Bothell, WA, USA). The morphometric parameters such as spheroid diameter and spheroid volume were calculated from the images using Image J analysis software.
b. **Cell Viability Assay** – % Cell viability of tumor spheroids was determined using Cell Titer-Glo™ 3D assay kit (Promega, Madison, WI, USA). Briefly, at the end of experiment (Day 6), 50 µL of Cell Titer-Glo® 3D reagent was added in each well after removing 150 µL of media (n=3 for each treatment group). After incubation of 30 minutes, the luminescence signal was measured using TECAN plate reader (Tecan Group Ltd., Männedorf, Switzerland). The % cell viability was calculated for each treatment group by comparing the viability against control.
c. **Viable Cell Imaging** – Viable cell imaging of the tumor spheroids was performed on day 6 using calcein AM dye (Biotium, Fremont, CA, USA) which stains the viable cells with green florescence. Briefly, 100 µL of florescent dye was added to each well after carefully aspirating the treatment, followed by 30 minutes of incubation in dark.

www.manaraa.com

Labeled spheroid cells were imaged using EVOS FL florescence microscope (Thermo Fisher Scientific, Waltham, MA, USA) at 4X magnification.

3.13 Evaluating Impact on Cardiotoxicity of DOX

3.13.1 Lactate Dehydrogenase (LDH) Assay

Cardioprotective effect of DOX-conjugated particles as against free DOX was evaluated in H9c2 rat cardiomyoblasts using LDH assay. LDH-Glo™ cytotoxicity assay (Promega, Wisconsin, MI, USA) kit was used to evaluate the toxicity of free DOX and DOX-conjugated particles by measuring the LDH released from the cytosol due to loss of membrane integrity of the cells. Briefly, H9C2 cells were plated in 24 well tissue culture plates at 8.0×10^4 cells/well density and were incubated overnight at 37°C/5%CO_2. Following incubation, the cells were treated with 1.25 µM concentration of free DOX and DOX-conjugated particles for 24 hours. Subsequently, the cells were treated with reagents of LDH-Glo™ Cytotoxicity Assay (Promega, Wisconsin, MI, USA) as per the manufacturer's instructions. The luminescence of the treatment groups was measured using TECAN plate reader.

3.13.2 Apoptosis Evaluation- Acridine Orange/Ethidium Bromide (AO/EB) Staining

DOX is known to induce apoptosis as one of the pathways to induce the cardiotoxicity. Therefore, to evaluate the influence of DOX-conjugated particles in providing protection against DOX induced apoptosis in H9C2 rat cardiomyoblasts, acridine orange (AO) and ethidium bromide (EB) double florescent staining method as reported previously was used [69]. Briefly, H9C2 cells were seeded at a density of 8.0×10^4 cells/well in a 24 well tissue culture plate and incubated overnight at 37°C/5% CO_2 overnight. Post incubation, the cells were treated with free DOX and DOX-conjugated

www.manaraa.com

particles at a concentration of 1.25 µM for 24 hours. After the treatment period, cells were washed twice with PBS pH 7.4 and stained using 200 µL of 1:1 AO:EB at concentration of 100µg/mL each. The cells were incubated with dyes in dark for 30 minutes and imaged at 20X magnification using EVOS-FL florescence microscope (Thermo Fisher Scientific, Waltham, MA, USA)

3.15 Statistical Analysis

All the results are presented as mean±SD unless otherwise stated. Statistical significance was determined using student's t-test, one-way ANOVA and Tukey's post-hoc multiple comparison by GraphPad Prism 6.01 (San Jose, CA, USA). $p<0.05$ or less was considered significant.

www.manaraa.com

4.0 Results and Discussion

4.1 Particle Fabrication and Morphology of Particles

Three different sizes of polystyrene particles were used to prepare elongated rod-shaped (fiber like) particles. The rod-shaped particles were successfully fabricated using one-dimensional film stretching as mentioned in the methods section. The particles were imaged using SEM as seen in **Figure 6**, spherical particles over various sizes were successfully transformed to rod shaped particles having varied aspect ratios. Aspect ratio (AR) is defined as the ratio of the length of major axis of particles to the length of minor axis of the particles. As seen from **Table 1 and Figure 6**, stretching of 0.5μm particles to 3 folds resulted into short rod (SR) shaped particles with major axis of 1.4 ± 0.1 μm and minor axis 0.3 ± 0.0 μm resulting into AR of 4.08 ± 0.17. Upon further stretching the particles to 6-fold, of 0.5μm particles produced particles long rods (LR) having major axis length of 1.9±0.2 μm and minor axis length of 0.3 ± 0.0 μm possessing an AR value of 6.56 ± 0.60. As observed increase in stretching length from SR to LR resulted into increase in AR value. Similarly, polystyrene particles of 6.0 μm equivalent diameter upon 3 folds stretching resulted into SR with 9.1±0.9 μm (major axis length) and 1.7±0.3 μm (minor axis length) causing an AR value of 5.4±0.8. Further, LR of 6.0 μm equivalent diameter displayed 13.7±1.6 μm (major axis length) and 1.5±0.4 (minor axis length) resulting into 9.14 ± 1.42 AR value **(Table 1 and Figure 6)**.

www.manaraa.com

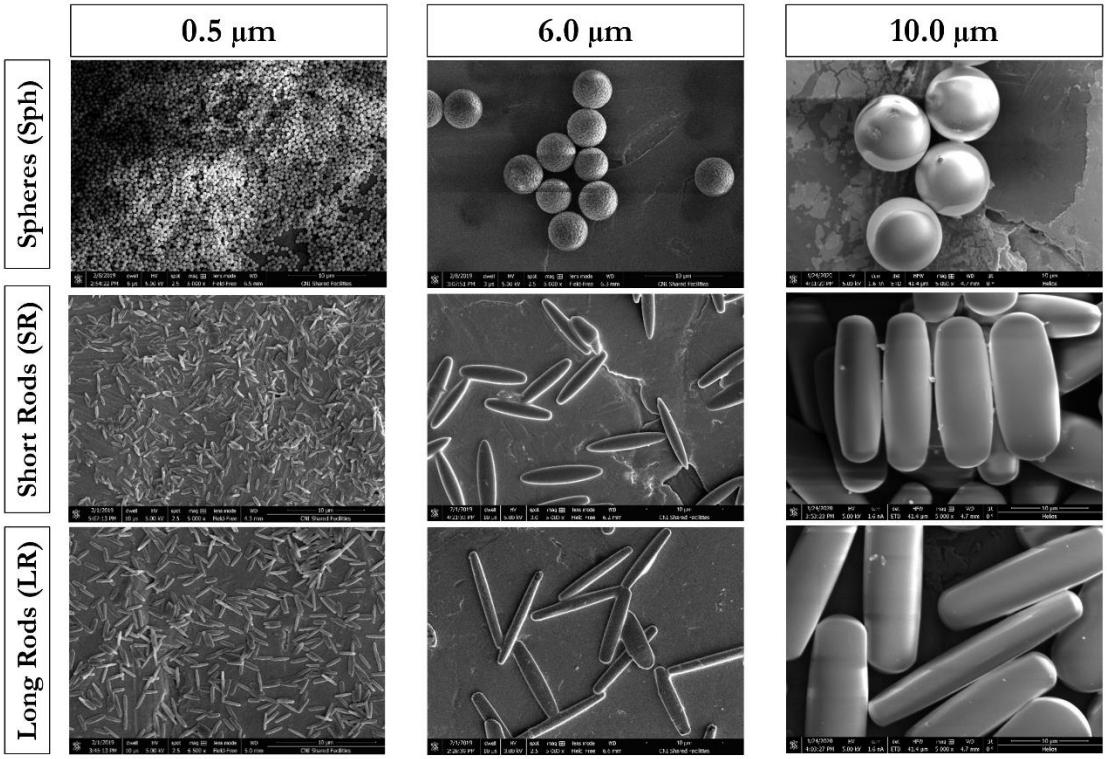

Figure 6: Representative scanning electron microscopy (SEM) micrographs of particles obtained by stretching microparticles of various sizes. Scale bar= 10µm

Table 1: Calculated particle size of stretched particles using Image J software. Data represents mean±SD for 3 individual images with n=30 for each sample**.**

Sample	Major axis length (µm)	Minor axis length (µm)	Aspect Ratio (Major axis/Minor axis)
0.5µm-SR	1.4 ± 0.1	0.3 ± 0.0	4.1 ± 0.2
0.5µm-LR	1.9 ± 0.2	0.3 ± 0.0	6.6 ± 0.6
6.0µm-SR	9.1 ± 0.9	1.7 ± 0.3	5.4 ± 0.8
6.0µm-LR	13.7 ± 1.6	1.5 ± 0.4	9.1 ± 1.4
10µm-SR	22.1 ± 3.3	7.1 ± 0.9	3.3 ± 0.5
10µm-LR	32.2 ± 3.2	5.6 ± 0.9	5.8 ± 1.1

www.manaraa.com

Stretching of 10.0 µm particles to 3 folds resulted into fabrication of SR particles with 22.1 ± 3.3 µm major axis length and 7.1 ± 0.9 µm of minor axis length accounting for AR value of 3.3 ± 0.5. Similarly, stretching to 6 folds formed LR particles with 32.2 ± 3.2 µm (major axis length) and 5.6 ± 0.9 µm (minor axis length) resulting into 5.8 ± 1.1 AR value as can be seen in **Table 1 and Figure 6**. Interestingly it was observed that AR values of both SR and LR particles stretched from10.0 µm equivalent diameter size was found to be less than their respective counterparts of 6.0 µm and 0.5 µm equivalent diameter size particles. This reduction in the AR value of 6.0 and 10.0 µm equivalent diameter particles as against 0.5 µm can be attributed to the crosslinking of the polystyrene particle; as these large sized particles were reported to be crosslinked with divinylbenzene (Manufacturer protocol, Polysciences Inc.). Polymer crosslinking is known to restrict the rotational motion of the polymer molecules resulting into increase in the glass transition temperature of polymer which increases the rigidity of the polymer [70]. The increased rigidity of the polymer hampers the flexibility of the particle to be stretched and thus resulting into lower AR values. These results infer that particle of various size can be successfully transitioned from spherical to rod shape by employing the stretching method.

4.2 Conjugation of Drug with Particles

DOX was chosen as the model drug for conjugation with the particles due to the 2 major reasons : 1) widely explored conjugation chemistry and 2) inherent florescence which can be used in the *in-vitro* studies. The fabricated particles were conjugated with DOX using EDC-NHS chemistry and the amount of DOX-conjugated was analyzed by measuring UV absorbance. As seen in **Figure 7**, the amount of DOX-conjugated to particles of 0.5 µm size was found to be 454.6 ± 2.0 µg of DOX/mg of particles (Sph),

www.manaraa.com

469.1 ± 5.3 µg of DOX/mg of particles (SR) and 425.8 ± 5.5 µg of DOX/mg of particles (LR). Upon increasing the particle size from 0.5 to 6.0 µm, the amount of DOX-conjugated/mg of particles remained almost same as in **Figure 7**.

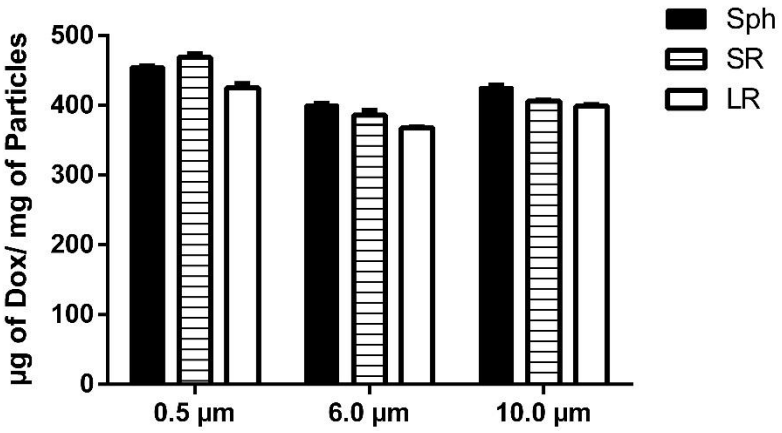

Figure 7: Characterization of DOX conjugation to various 10µm particles. (A) amount of DOX-conjugated to various particles expressed as µg of DOX/mg of particles. Data is represented as mean±SD for n=3 experiments.

6.0µm-Sph showed 400.1 ± 2.6 µg of DOX/mg of particles while stretched particles displayed 386.2 ± 6.5 µg of DOX/mg of particles (6.0µm-SR) and 367.7 ± 1.7 µg of DOX/mg of particles (6.0µm-LR). Further increasing the particle size to 10µm, conjugation of DOX was found to be unaffected with 10µm-Sph illustrating 425.5 ± 3.3 µg of DOX/mg of particles. The stretched particles 10µm-SR displayed 406.1 ± 1.2 µg of DOX/mg of particles while 10µm-LR demonstrated 399.0 ± 1.9 µg of DOX/mg of particles being conjugated (**Figure 7)**. The amount of DOX-conjugated to carboxylic acid groups functionalized on particles across various size and shape almost remained similar. This indicates that carboxylic acid functionalized on the surface of polystyrene particles remain unaffected by the stretching owing to its hydrophilic nature and thus are believed to be readily available for conjugation. The amount of carboxylic acid groups available for

www.manaraa.com

conjugation on particles is attributed to be dependent on the total particle volume indicating that increase in size of particle causes increase in amount of carboxylic acid groups [71]. Therefore, to equalize the amount of carboxylic acid available for conjugation amongst the particles various size and shapes, we have used a constant total mass of particles for conjugation reaction. This values of µg of DOX/mg of particles were found to be almost equivalent as seen in **Figure 7.**

4.3 Characterization of DOX Conjugation

4.3.1 DSC Studies

Calorimetric studies was performed to evaluate the conjugation of DOX with the particles. **Figure 8A** represents the thermogram of the analyzed samples, wherein DOX shows a sharp endothermic peak at 206.2°C representing the melting of DOX as also reported in literature [72,73]. Thermogram of blank particles displays a small endothermic peak at 103.2°C representing the glass transition (T_g) temperature of polystyrene [74,75]. Thermal study result of physical mixture of DOX and blank particles demonstrate first endothermic peak at 105.3°C due to T_g of blank particles and second at 198.4°C representing melting point of DOX as in **Figure 8A**. In case of all the DOX-conjugated particles, the characteristic peak of DOX was found to be absent, indicating that pure DOX was not present in the conjugated particles and was removed during washing steps suggesting that DOX present in the formulation is bound to the particles. These results also indicate that DOX was bound strongly to the particles resulting into formation of a stable bond [73].

www.manaraa.com

(A)

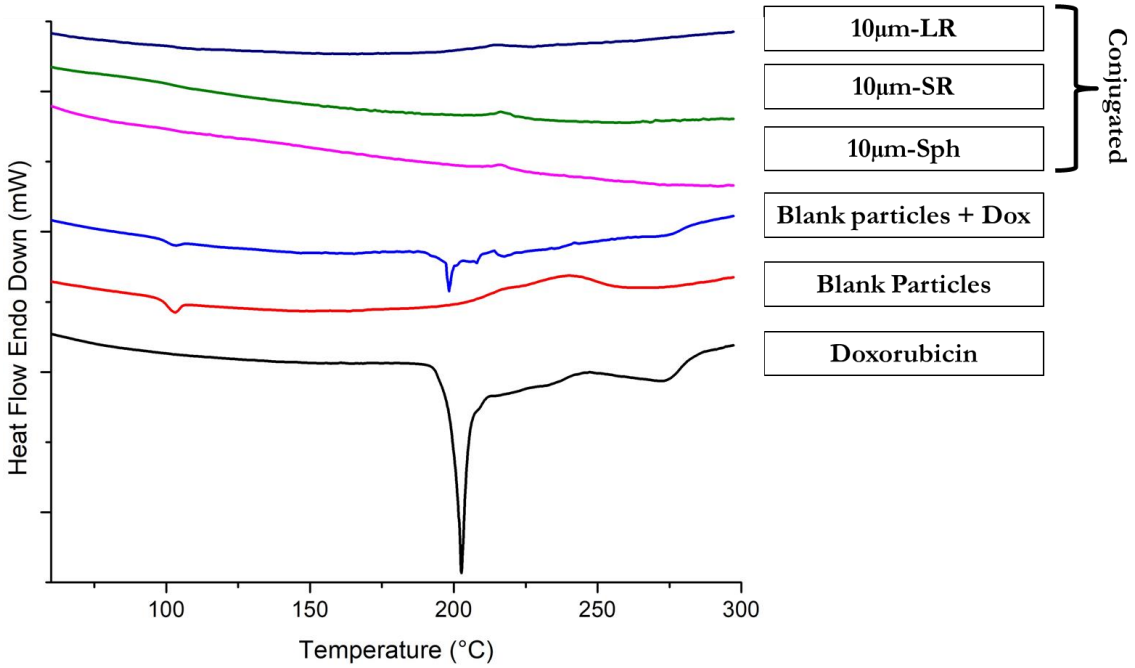

(B)

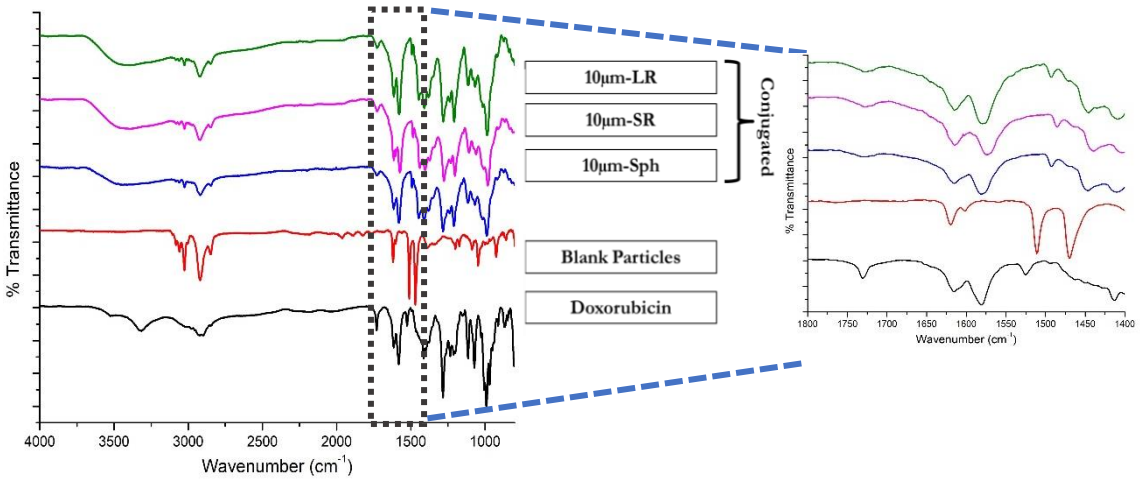

Figure 8: Characterization of DOX conjugation to various 10µm particles. (A) Thermograms of samples analyzed using differential scanning calorimetry (DSC). (B) Spectra of samples analyzed using FT-IR also a representative magnified image of spectra is shown for all the samples.

www.manaraa.com

4.3.2 FT-IR studies

Thermal spectra of analyzed samples are displayed in **Figure 8B** wherein DOX displays several characteristic peaks at 3315 cm^{-1} (-N-H_2 stretching), 2916 and 2898 cm^{-1} (-C-H stretching of phenol rings), 1730 cm^{-1} (-C=O ketone stretching and C-H_2 bending), 1617 cm^{-1} (-CO-H bending), 1580 cm^{-1} (-C=O quinone stretching), 1525 cm^{-1} (out of pane vibration of -N-H_2) and 881 cm^{-1} (-C-N bending) [76–78]. Polystyrene particles demonstrated peaks at 3106 cm^{-1}, 3079 cm^{-1} and 3026 cm^{-1} (C-H stretching of aromatic rings and -O-H stretching of carboxylic acid), 2930 cm^{-1} and 2849 cm^{-1} (-CH_2- stretching), 1620 cm^{-1} ,1511 cm^{-1} and 1470 cm^{-1} (C=C stretching of aromatic rings) [79,80] (**Figure 8B)**. Analysis of all the three DOX-conjugated particles (10µm-Sph, 10µm-SR and 10µm-LR) demonstrated majority of characteristic peaks of DOX at ~ 3315 cm^{-1}, 2916 cm^{-1}, 1730 cm^{-1} and 1580 cm^{-1} indicating the presence of DOX in the conjugated particles. However, as seen in **Figure 8B** conjugation of DOX to polystyrene resulted into substitution of 1525 cm^{-1} (out of pane vibration of -N-H_2) of DOX with peak at 1509 cm^{-1} (10µm-Sph), 1502 cm^{-1} (10µm-SR) representing amide II vibrations of -N-H and -C-N stretching, indicates the involvement of -NH_2 group to form the -CONH bond [81,82]. These FT-IR results indicates successful conjugation of DOX to the polystyrene particles via amide bond linkage between the carboxylic acid (-COOH) groups of polystyrene particles and amine (-NH_2) group of DOX

4.4 *In-vitro* Pulmonary Deposition Behavior

The aerodynamic behavior of the fabricated particles were assessed using NGI measured in terms of MMAD and % FPF. The data of the impact of particle shape and size on *in-vitro* pulmonary deposition is shown in **Table 2.**

www.manaraa.com

Table 2: Aerosolization properties of various microparticles calculated in terms of MMAD and % FPF. Data is represented as mean±SD for n=3 experiments. *p<0.05, ** p<0.01, **** p<0.001 and **** p<0.0001.

Sample	MMAD	% FPF
0.5µm-Sph	4.5 ± 0.3	77.2 ± 5.0
0.5µm-SR	4.2 ± 0.5	74.2 ± 0.7
0.5µm-LR	4.4 ± 0.4	79.5 ± 5.7
6.0µm-Sph	5.6 ± 0.1	61.7 ± 2.1
6.0µm-SR	4.3 ± 0.2**	76.5 ± 4.9*
6.0µm-LR	4.7 ± 0.1**	76.2 ± 1.1*
10µm-Sph	8.2 ± 0.8	44.7 ± 5.7
10µm-SR	4.2 ± 0.6****	89.5 ± 9.6***
10µm-LR	3.4 ± 0.1****	95.5 ± 0.6****

Aerodynamic parameters of 0.5 µm particles assessed using NGI are shown in **Table 2**. All the three particles; 0.5µm-Sph, 0.5µm-SR and 0.5µm-LR demonstrated MMAD ~4.5 along with no significant difference observed in % FPF value reported to be >75%. Increase in the particle size from 0.5 µm to 6.0 µm resulted into increase in the MMAD of 5.6 ± 0.1 (for 6.0µm-Sph) along with % FPF value of 61.7 ± 2.1 indicating maximum deposition occurring the proximal region of the respiratory tract. However, transition of particle shape from spheres to rod resulted into significant (p<0.01) reduction in MMAD value as 4.3 ± 0.2 for 6.0µm-SR and 4.7 ± 0.1 as observed for 6.0µm-LR (**Table 2)**. On the other hand, % FPF values for 6.0µm rod shaped particles were found to be significantly (p<0.05) increased as against the spherical particles as seen in **Table 2**. 6.0µm-SR resulted into 76.5 ± 4.9 % FPF value and 6.0µm-LR displayed 76.2 ± 1.1 % FPF

www.manaraa.com

value. Similarly, MMAD value for 10µm-Sph as reported in **Table 2** indicated a high MMAD value of 8.19±0.8 µm while the stretched particles demonstrated a significantly (p<0.0001) lower MMAD values of 4.2 ± 0.6 µm for 10µm-SR particles and 3.4 ± 0.1 µm for 10µm-LR particles, respectively. Upon comparing the % FPF value (**Table 2**), 10µm-Sph displayed ~45% while rod-shaped particles demonstrated significant (p<0.0001) increase in % FPF with ~90% for 10µm-SR and ~95% for 10µm-LR particles. This increase in % FPF indicates that most of the emitted dose will be deposited in the respirable region of the lungs which comprises of the bronchi-alveolar region.

The deposition of 10µm DOX-conjugated particles on various stages of NGI are represented in **Figure 9A**. As can been seen from the **Figure 9A**, for 10µm-Sph particles, the deposition was seen mostly in stage 1 (~4 µg), stage 2 (~ 6 µg), stage 3 (~5 µg) and stage 4 (~3 µg) while ≤ 1 µg DOX deposition was observed from stage 5 to stage 8. This indicated that deposition of 10µm-Sph predominantly occurred above the bronchi-alveolar regions. The stretched particles: 10µm-SR and 10µm-LR on the other hand showed minimal deposition at stage 1 and 2 (≤ 1 µg). The deposition of stretched particles, both SR and LR increased dramatically stage 3 onwards. Maximum deposition of particle for stretched particles was observed in stage 5 wherein ~ 22 µg of DOX was quantified for 10µm-SR and ~28 µg DOX for 10µm-LR particles. At stage 6, the deposition of DOX decreased to ~16 µg for 10µm-SR while the reduction in deposition behavior of 10µm-LR particles was mild with ~25 µg DOX observed for 10µm-LR. The deposition of 10µm-LR particles as could be seen in **Figure** 9**A** continued until stage-8 with ~5 µg DOX observed while the 10µm-SR particles displayed ~0.5 µg DOX.

www.manaraa.com

(A)

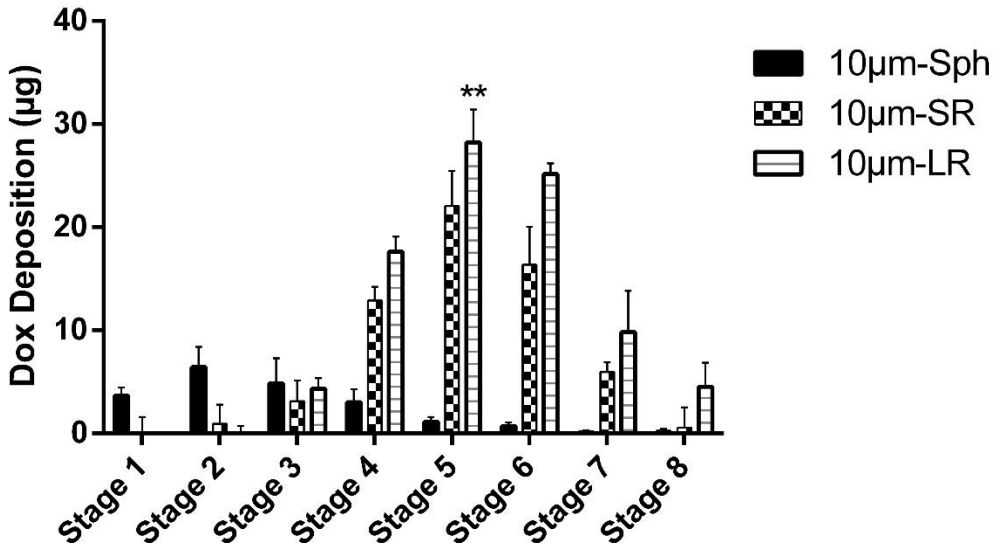

(B)

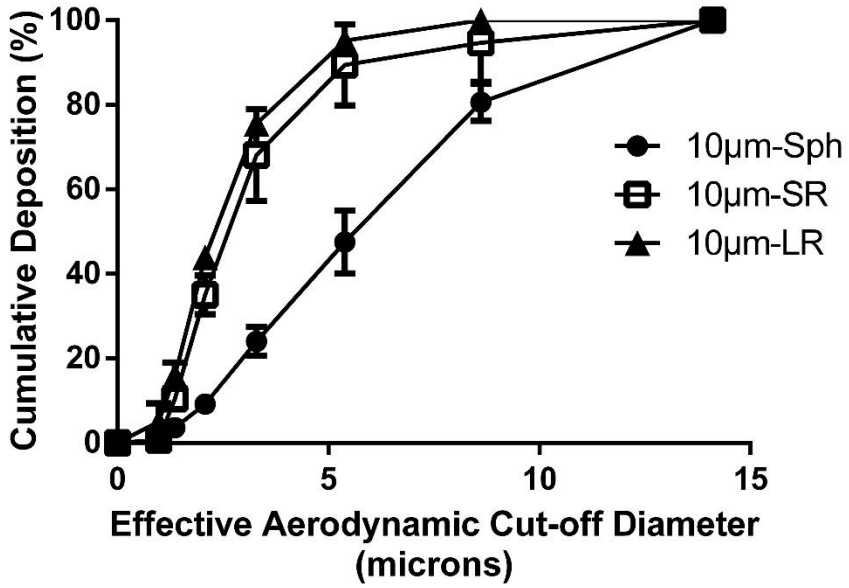

Figure 9: (A) Aerodynamic distribution pattern of various 10µm particles at different stages of Next Generation Cascade Impactor (NGI) expressed as DOX Deposition (µg) at each stage. (B**)** % Cumulative deposition plotted against effective cut-off diameter (microns) to determine deposition impact due to difference in particle shape of 10µm particle. Data represents mean ± SD (n=3). ** $p<0.01$

www.manaraa.com

Since majority of deposition for 10µm-SR and 10µm-LR stretched particles beyond stage 3 (representing bronchi-alveolar region), it can be confirmed that change in the shape of the particles enhance the deposition of particles in the deeper lungs. The % cumulative deposition plot as in **Figure 9B** indicated that 50% of the cumulative dose for 10µm-Sph deposited at the effective cut-off aerodynamic diameter of 5.57 µm. The stretched particles demonstrated a significantly ($p<0.0001$) lower effective cut-off aerodynamic diameter for 50% cumulative deposition: 2.53 µm for 10µm-SR particles and 2.26 µm for 10µm-LR particles (**Figure 9B)**. These results support the fact that rod shaped particles (stretched particles) improve the deposition behavior of the particles as against the spherical particles resulting into maximum deposition at lower aerodynamic diameter. This can be attributed to the better propulsion of rod-shape particles down the respiratory tract after aligning themselves with the air flow [83]. Several computational fluid dynamics simulation models have predicted the deposition of fiber (elongated rod shaped; AR>3) vs sphere particles in the lungs, wherein elongated particles streamlines themselves to the air flow and therefore tend to deposit in the peripheral airways [83–85]. Particle shape is also reported to influence the mechanism of particle deposition in lungs; wherein the spherical particles tend to deposit predominantly by inertial impaction (for MMAD>5 µm), gravitational sedimentation (for MMAD 1 to 5 µm) or diffusion (for MMAD ≤0.5 µm) [34,37,86]. While the rod-shaped particle on the other hand deposit by interception, wherein the fiber like particles comes in close contact to the surface such that it touches the surface which would have been missed by the center of the mass [36]. Increase in the length of particles results into increase in the deposition of particles via interception which allows the particles to streamline with the airflow and travel to the distal airways in the alveolar region [87]. This

www.manaraa.com

justifies the improved aerodynamic behavior of rod-shaped particles against spheres and amongst the rod-shaped particles, LR better than SR. Therefore, the results of in-vitro pulmonary deposition behavior have been successful in supporting the hypothesis that changing the shape of spherical particles to rod-shape results into deeper lung deposition of particles.

4.5 *In-vitro* Release of DOX-conjugated Particles

The release of DOX from conjugated polystyrene particles was analyzed in buffers at pH 7.4 mimicking physiological conditions and pH 5.5 representing lysosomal vesicles and microenvironment of cancer cells [88,89]. As seen in **Figure 10**, no burst release of DOX was observed in the in-vitro release study. The release of DOX was observed to be pH dependent which indicated that release of DOX was faster at lower pH value of 5.5 as compared to higher pH 7.4. DOX-conjugated particles upon incubation at pH 5.5 released about 45.2 ± 2.8 % of DOX from 10µm-Sph particles, 43.8 ± 1.3 % DOX from 10µm-SR particles and 45.7 ± 1.3% DOX from 10µm-LR particles after 5 days (**Figure 10**). While significantly (p<0.0001) small amount of DOX was found to be released at physiological pH 7.4 due to slower hydrolysis of the amide bond [81]. The % drug released after 5 days incubation of 10µm-Sph particles was 18.9 ± 2.3% while 10µm-SR particles displayed 18.7 ± 3.0% and 10µm-LR particles showed 18.7 ± 3.7% cumulative release of drug (**Figure 10**). On the other hand, increased release of DOX from the particles at acidic pH is known to be mediated cleavage of the amide bond due to acid hydrolysis resulting into subsequent release of DOX in the media [81,88]. These results are in accordance to other studies wherein slower release of DOX at pH 7.4 indicated enhanced stability of amide conjugated DOX particles and its slower hydrolysis kinetics at normal physiological

www.manaraa.com

conditions [81,89–91]. In addition, the slower release of DOX at physiological pH supports the use of these conjugated particles as effective delivery carrier due to reduced loss of DOX while reaching the site of action resulting into low off-target side effects and increased tumor accumulation [92,93].

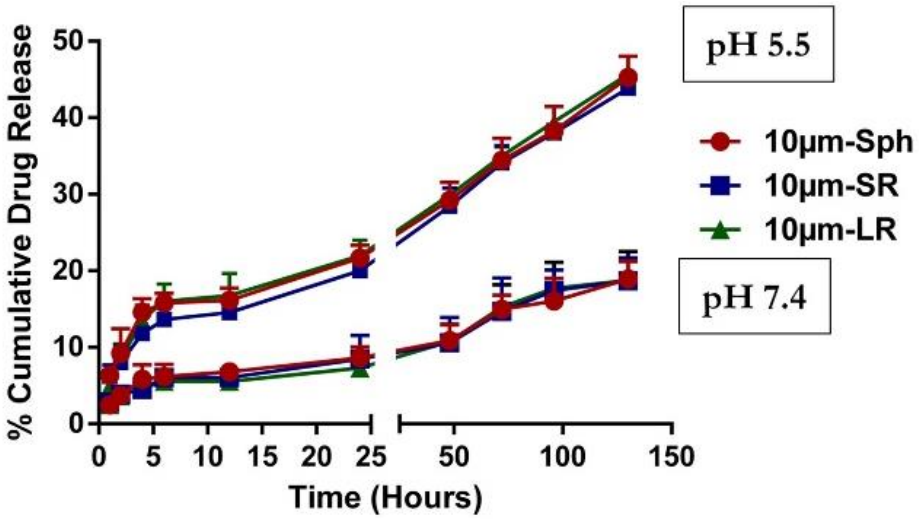

Figure 10: *In-vitro* drug release profile of DOX from various 10µm particles; 10µm-Sph, 10µm-SR and 10µm-LR evaluated at pH 7.4 and pH 5.5. Data represents mean ± SD (n=3).

4.6 Stability Studies

Stability of 10µm DOX-conjugated particles were tested after storing for 15 days at two different conditions: 1) storage conditions represented by 4°C and 2) accelerated stability conditions represented by 40°C and 75% relative humidity (RH). The stability was assessed in terms of particle shape, particle size and the amount of drug conjugated. **Figure 11A** represents the SEM images of the particles, wherein there was no change observed in the shape of the particles when stored at accelerated conditions as against normal storage conditions. This can be attributed to the high glass transition temperature (110°C) of the polystyrene particles remaining unaltered at the accelerated conditions (40°C/75% RH)

www.manaraa.com

and thereby maintain the same shape. Furthermore, the size of the stretched particles were measured using ImageJ software to evaluate if any existed in the particles. As seen in **Figure 11B**, the major axis of the 10µm-SR particles at 4°C was found to be 25.2 ± 1.2 µm (vs. 24.6 ± 1.9 µm at 40°C/75%RH) and minor axis of 24.6 ± 1.9 µm (vs. 7.9 ± 0.9 µm for 40°C/75%RH). The aspect ratio of particles also showed non-significant difference with 3.5 ± 0.4 at normal conditions vs. 5.9 ± 0.9 at accelerated condition. Similarly, 10µm-LR particles also displayed non-significant changes in particle size parameters as in **Figure 11B**. The length of major axis at 4°C was found to be 36.2 ± 2.0 µm while at 40°C/75%RH it was reported to be 36.7 ± 2.5 µm. The minor axis of 10µm-LR particles at normal conditions was found to be 6.1 ± 0.9 µm at vs. 5.9 ± 0.9 µm at accelerated conditions. Upon analyzing the aspect ratio values, no significant differences were observed between 4°C with 6.4 ± 1.0 compared to 6.3 ± 1.2 at 40°C/75%RH (**Figure 11B).**

Furthermore, the amount of conjugated to the particles was analyzed at the end of the stability period. As seen in **Figure 11C**, 10µm-Sph displayed 426 ± 10µg of DOX/mg of particles at 4°C as against 421 ± 9 µg of DOX/mg of particles at 40°C/75%RH. 10µm-SR particle demonstrated ~430 mg of µg of DOX/mg of particles at both the stability conditions. Similarly, 10µm-LR particle displayed non-significant changes with ~460 µg of DOX/mg of particles at both the stability conditions. This non-significant difference in the amount of conjugated drug present at both the stability conditions can be attributed to the stable amide bond conjugation between DOX and the carboxylic acid of the polystyrene particles which remains unaffected at the increased temperature [94]. These results indicate the superior stability of DOX-conjugated particles at the accelerated conditions.

www.manaraa.com

(A)

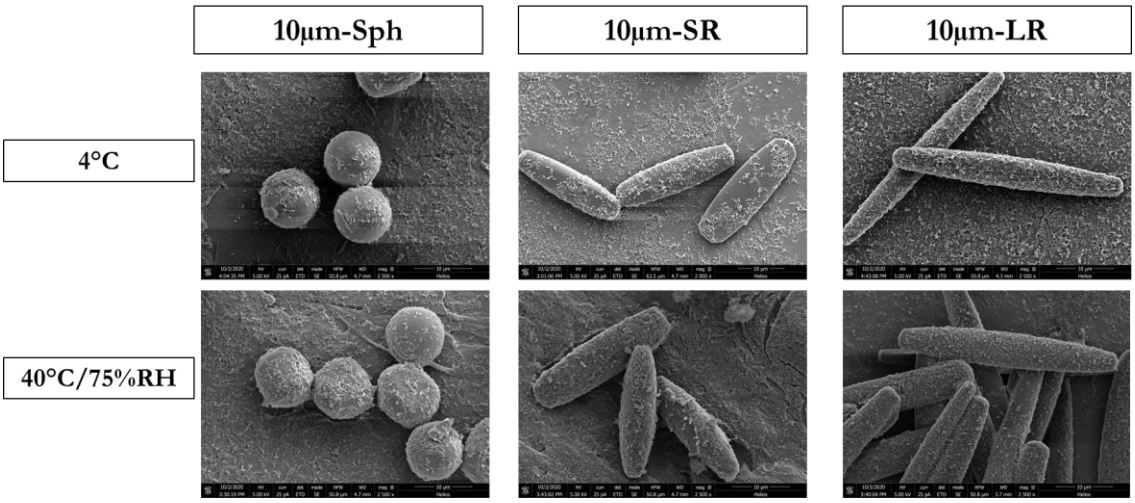

(B)

Particles	Major Axis (µm)		Minor Axis (µm)		Aspect ratio	
	4°C	40°C/75%RH	4°C	40°C/75%RH	4°C	40°C/75%RH
10µm-SR	25.2 ± 1.2	24.6 ± 1.9	7.2 ± 0.8	7.9 ± 0.9	3.5 ± 0.4	3.2 ± 0.5
10µm-LR	36.2 ± 2.0	36.7 ± 2.5	6.1 ± 0.9	5.9 ± 0.9	6.4 ± 1.0	6.3 ± 1.2

(C)

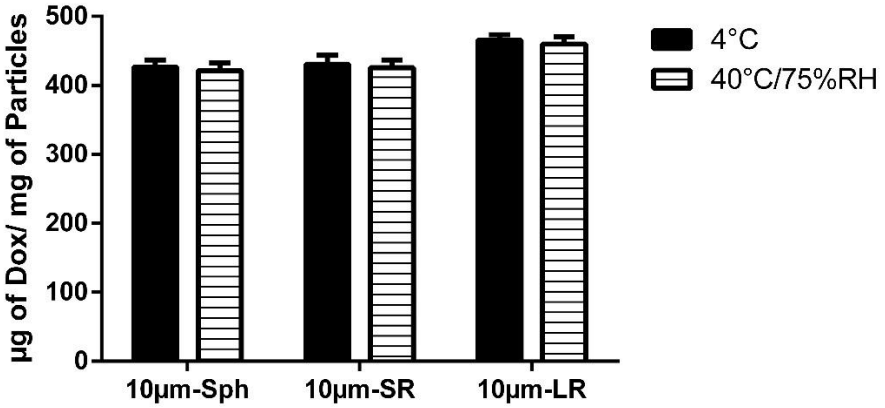

Figure 11: Stability of various 10µm particles evaluated at two different conditions; 4°C and 40°C/75%RH, after 15 days storage evaluated for changes in morphology, particle size, and amount of drug conjugated. (A) Stability evaluated in terms of morphological changes of particles represented by respective SEM micrographs. (B) Stability evaluated in terms of major axis length, minor axis length and aspect ratio of particles and (C) Stability evaluated in terms of µg of DOX/mg of particles present at the end of 15 days.

www.manaraa.com

4.7 Investigating Escape of Particles by Macrophages

4.7.1 Cellular Uptake

The cellular uptake of DOX-conjugated spherical and stretched particles was analyzed using fluorescent microscope after incubation of particles for 3 hr. As seen in **Figure 12A**, DOX demonstrated enhanced internalization with DOX florescence (Red) being overlapped over the cellular nuclei (DAPI- blue fluorescence). This indicates that free DOX was readily localized in the cell nucleus of RAW 264.7 cells. For 10µm-Sph particles, it can be observed that DOX was conjugated to the spherical particles and distributed in the cytoplasm surrounding the nuclei of RAW 264.7 cells. The stretched particles 10µm-SR displayed presence of some DOX particles in the cytoplasm of the cells, however the florescence intensity of DOX was comparatively less than the spherical particles indicating reduced cellular uptake of the 10µm-SR stretched particles (**Figure 12A)**. For 10µm-LR particles as in **Figure 12A**, there was minimal DOX florescence observed in the cytoplasm or nuclei of the cells suggesting impact of particle shape on the cellular uptake by the macrophage cells. Based on these results, it can be inferred that change in the shape of the particles may influence the uptake of the particles by macrophages.

The intracellular uptake of free DOX and DOX-conjugated particles was analyzed by quantifying the florescence of DOX. As demonstrated in **Figure 12B**, free DOX displayed the highest florescence intensity at both the incubation time; 1 hr. and 3 hrs. Furthermore, free DOX demonstrated significantly ($p<0.001$) stronger florescence intensity than 10µm particles (spherical and stretched) at both 1 hr. and 3 hrs. incubation time.

www.manaraa.com

(A)

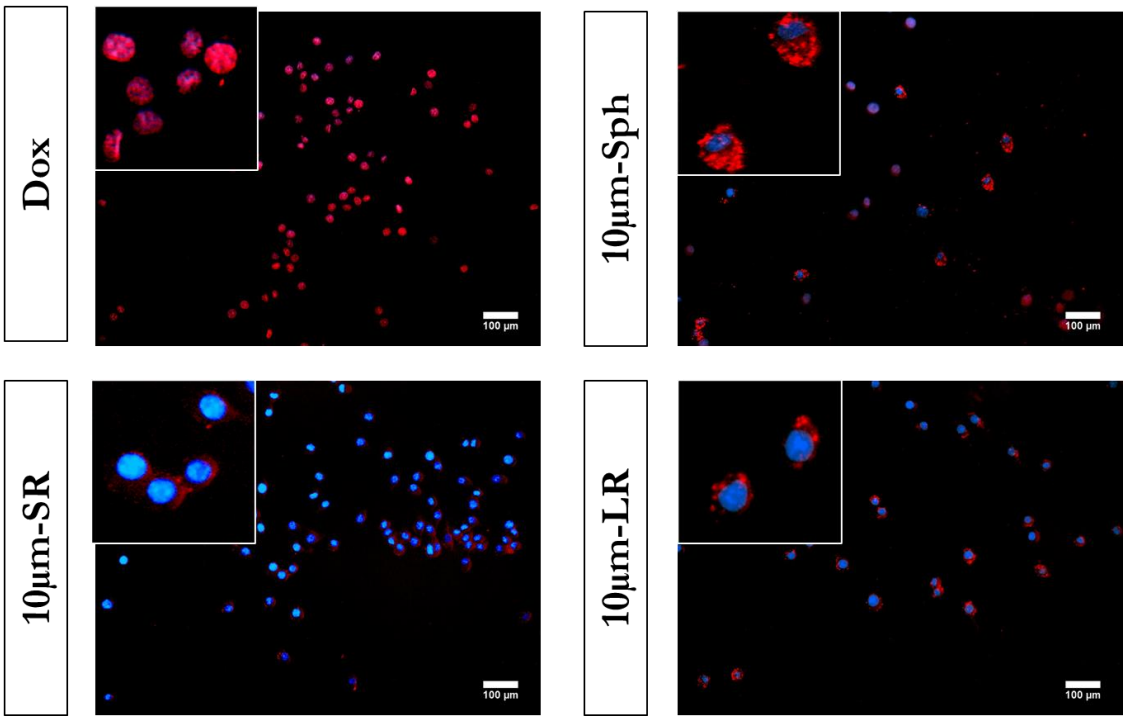

(B)

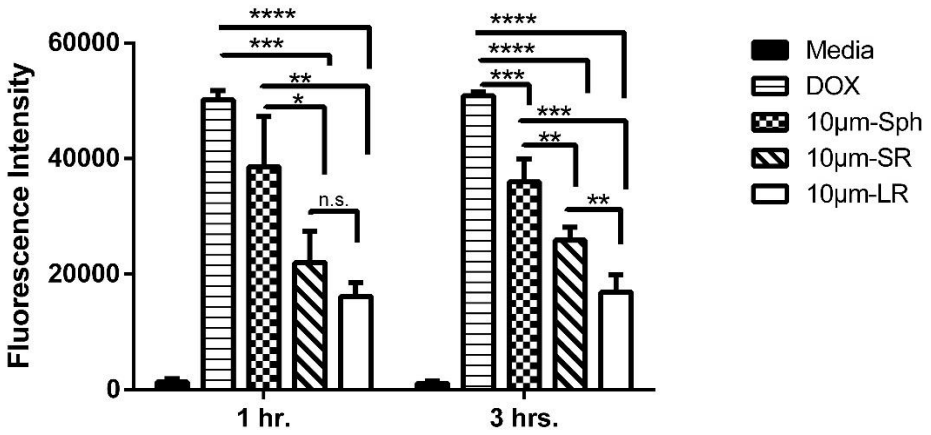

Figure 12: *In-vitro* cellular uptake studies of various 10µm particles. (A) Florescent images of DOX, 10µm-Sph, 10µm-SR and 10µm-LR in RAW 264.7 macrophages after 3 hrs. incubation. The inset images represents magnified image of the outside image. Representative images from n = 3 experiments. Scale bar = 100 µm (B) Quantitative determination of intracellular DOX after 1 hr. and 3 hrs. incubation in RAW 264.7 cells represented as florescence intensity. Data represent mean ± SD (n=3). *p<0.05, ** p<0.01, **** p<0.001 and **** p<0.0001.

www.manaraa.com

Amongst, 10um particles Sph demonstrated significantly higher florescence intensity after 1 hr. incubation ~1.7-folds ($p<0.05$) and ~2.4 folds ($p<0.01$) than 10µm-SR particles and 10µm-LR particles, respectively. However, at 1 hr. incubation there was no significant difference observed between the fluorescence intensity of 10µm-SR particles and 10µm-LR particles. The florescence intensity of 10µm-sphere particles after 3 hrs. incubation displayed ~1.4 folds ($p<0.01$) increased florescence intensity as against 10µm-SR particles while ~2.4 folds ($p<0.001$) increase as compared to 10µm-LR particles as in **Figure 12B**. Additionally, 10µm-SR particles displayed significantly ($p<0.01$) higher fluorescence of ~1.5 folds when compared to 10µm-LR particles. The results of this study are also corroborated by the fluorescence imaging results depicting the escape of 10µm-LR particles from macrophage uptake.

The enhanced internalization of free DOX in the macrophages can be attributed to the rapid passive diffusion mechanism of DOX [95,96]. Whereas internalization of DOX-conjugated 10µm particles (both spheres and stretched particles) may undergo energy dependent uptake pathway such as phagocytosis and therefore display comparatively reduced uptake as against DOX [97]. The results further demonstrate that change in the shape of the particle from sphere to rod results into reduced uptake by macrophages. This in accordance to several studies reporting that macrophage uptake is highly influenced by the shape of particles wherein spherical particles are readily internalized as compared to non-spherical shape [61,98,99]. This effect is further escalated for particles with higher aspect ratio, wherein macrophages are not able to completely engulf such particles due to incomplete formation of actin pseudopods around the particles resulting into reduced

www.manaraa.com

cellular internalization [99,100]. Therefore, particles with higher aspect ratio have higher possibility to escape the macrophage uptake which in our case is 10µm-LR particles.

4.7.2 Cytotoxicity Assessment on Macrophages

Cytotoxicity of free DOX and DOX-conjugated 10µm particles (Sph, SR, and LR) was assessed on RAW 264.7 cells using MTT assay after 24 hrs. and 48 hrs. incubation time. **Figure 13A** represents the % cell viability of RAW 264.7 cells after 24 hrs. treatment wherein free DOX demonstrated highest cytotoxicity of macrophages amidst all the treatment group with an IC_{50} value of 1.06 ± 0.1µM. The DOX-conjugated spherical particles at 5µM concentration displayed ~70% cell viability while stretched particles SR and LR displayed ~75% cell viability (**Table 3)**. Further, DOX displayed time dependent cytotoxicity on macrophages as can be observed in **Figure 13B and Table 3** with IC_{50} value of 0.08 ± 0.03 µM. The treatment with DOX-conjugated 10µm-Sph displayed ~28 folds increase in IC50 value; 2.8 ± 0.8 µM as compared to DOX. The stretched 10µm-SR particles displayed ~31 folds increase in IC50 value as compared to free DOX and ~1.1 folds increase against 10µm-Sph with an IC_{50} of 3.1 ± 0.1 µM. Treatment with 10µm-LR particles resulted into significant ($p<0.01$) ~71 folds increase in IC_{50} against DOX with IC_{50} of 7.5 ± 3.1 µM. Additionally, 10µm-LR particles displayed ~2.7 folds ($p<0.05$) increase in IC_{50} as against 10µm-Sph and ~2.5 folds ($p<0.05$) increase against10µm-SR particles (**Figure 13B and Table 3)**. Based on the cytotoxicity results, treatment group can be in the ranked in the following order for displaying cytotoxicity against RAW 264.7 macrophages: DOX>10µm-Sph>10µm-SR>10µm-LR. These outcomes are in accordance the results of cellular uptake wherein DOX is demonstrated to be readily internalized by macrophages via diffusion causing higher cytotoxicity.

www.manaraa.com

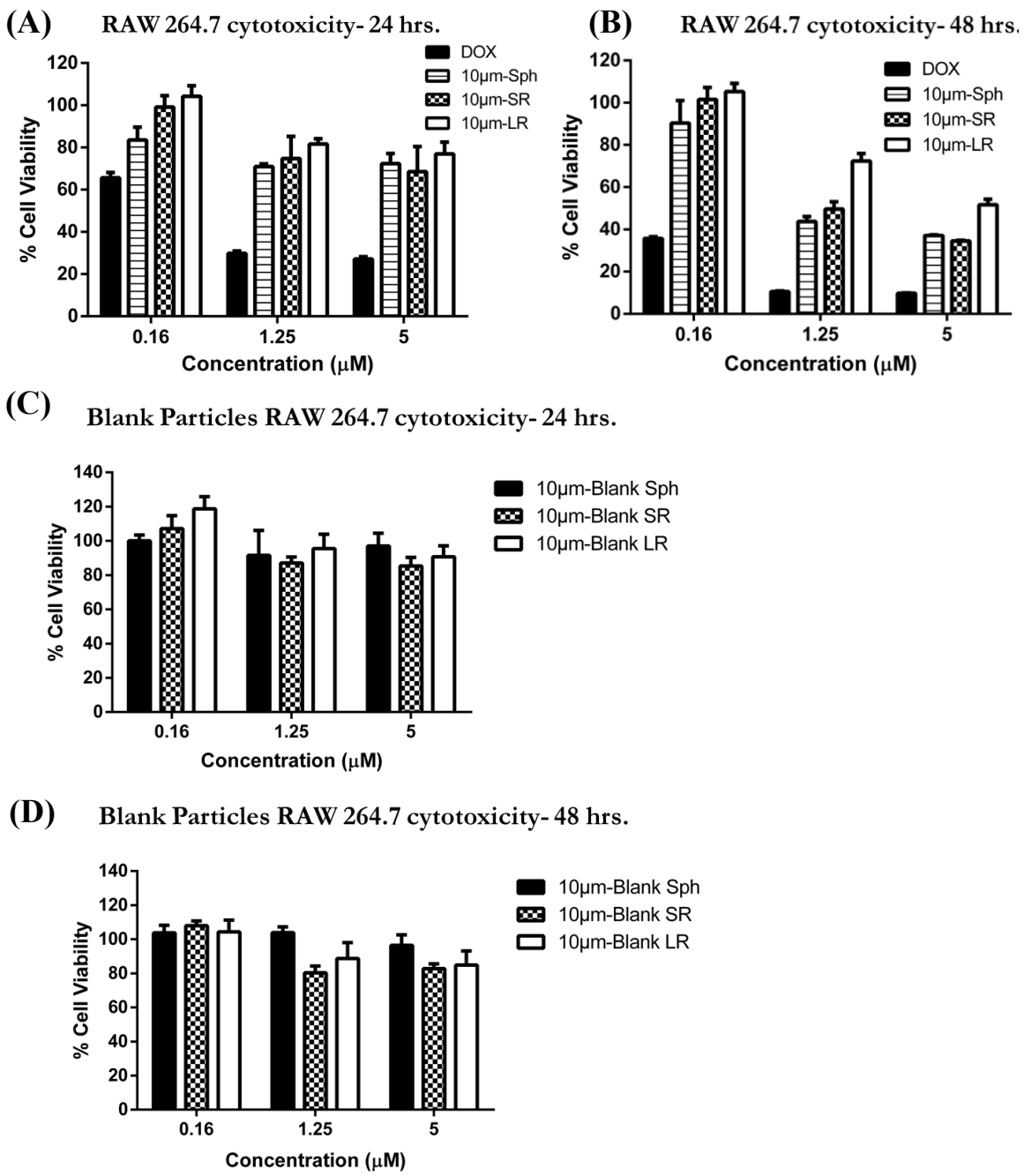

Figure 13: In-vitro *cytotoxicity studies of various 10µm particles in RAW 264.4 cells determined using MTT assay.* (A) Cytotoxic potential of DOX conjugated DOX-conjugated 10µm particles evaluated after 24 hrs. incubation (B) Cytotoxic potential of DOX conjugated DOX-conjugated 10µm particles was evaluated after 48 hrs. incubation (C) Blank particle cytotoxicity evaluated in RAW 264.7 cells after 24 hrs. incubation and (D) Blank particle cytotoxicity evaluated in RAW 264.7 cells after 48 hrs. incubation. (Data represent mean ± SD of 3 individual experiments with n=6 for each experiment).

www.manaraa.com

Amongst DOX-conjugated 10µm particles, stretched particle with highest aspect ratio i.e., 10µm-LR particles escape the cellular uptake by macrophages and thereby demonstrate significantly reduced cytotoxicity. The cytotoxicity of blank particles was also assessed in Raw 264.7 cells after 24 hrs. and 48 hrs. incubation. As seen in **Figure 13C**, after 24 hrs. of incubation all the blank particles demonstrated >85% cell viability. Similar results were observed after 48 hrs. incubation of particles as in **Figure 13D**, wherein all the particles displayed >80% cell viability against the macrophages indicating that the particles were safe against the RAW 264.7 cells. These findings indicate that the cytotoxicity of DOX-conjugated particles observed in macrophages is because of DOX from the conjugated particles internalized by the cells and not due to the polystyrene particles.

Table 3: IC_{50} values of different treatment groups in RAW 264.7 cells calculated from experimental cytotoxicity data obtained after 48 hrs. incubation

Treatment Group	**IC_{50} value (µM)**
DOX	0.1 ± 0.0
10µm-Sph	2.8 ± 0.8
10µm-SR	3.1 ± 0.1
10µm-LR	7.5 ± 3.1

4.8 Evaluating Impact of Particle Shape Against Small Cell Lung Cancer (SCLC)

SCLC was chosen as a model disease to predict the impact of particle shape of delivery carriers on the effectiveness of treatment. Lung cancer is known to be second most

www.manaraa.com

common cancer accounting for ~2 million death worldwide [101]. SCLC represents about 13% to 15% of the total lung cancer cases and is referred as the most aggressive form of lung cancer [102]. In this project, multidrug (including DOX) resistant H69AR SCLC cells were used to evaluate the efficacy of treatment against the tumorigenic property of SCLC cells. The reason to use DOX resistant H69AR cell line was the extremely low IC_{50} of DOX ~0.7 µM in the non-drug resistant variant H69 [103,104]. We believed that treatment of cells with DOX-conjugated particles at such low concentration may not will lead to extremely small number of particles being exposed to cells which may not truly reflect the effectiveness of particle shape on treatment against tumorigenic activity of cells

4.8.1 Cellular Uptake

The uptake of DOX-conjugated particles was assessed in DOX resistant SCLC cells after incubation for 3 hours using florescence microscope. As seen in **Figure 14A**, DOX (red florescence) was seen to be readily up taken by the cells and was localized in the nucleus (blue florescence). When DOX-conjugated particles were incubated with the cells, the florescence was observed in the cytoplasm of the cells unlike the free DOX which was localized in nucleus. The stretched particles displayed higher DOX florescence in the cytoplasm around the cells as compared to the 10µm sphere particles. Amongst the stretched particles, 10µm-LR particles displayed greater florescence than 10µm-SR particles (**Figure 14A**).

www.manaraa.com

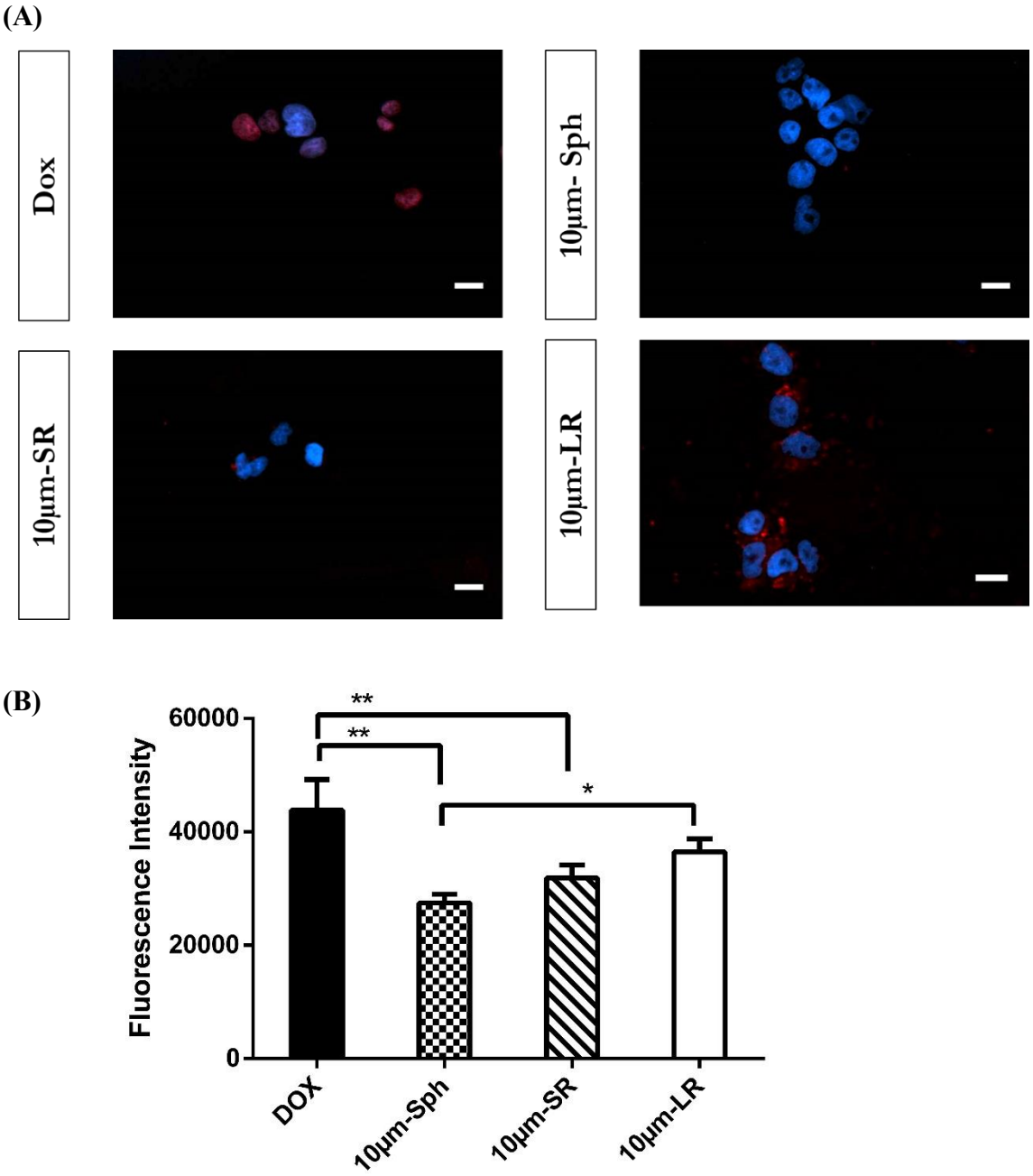

Figure 14: Cellular uptake studies of DOX-conjugated 10µm particles in H69AR cells after 3 hrs. incubation. Florescent images of DOX, 10µm-Sph, 10µm-SR and 10µm-LR in H69AR cells. Representative images from n = 3 experiments. Scale bar = 100 µm (B) Quantitative determination of intracellular DOX after 3 hrs. incubation in H69AR cells represented as florescence intensity. Data represent mean ± SD (n=3). *$p<0.05$ and ** $p<0.01$.

www.manaraa.com

In addition to florescence imaging, we have also evaluated cellular uptake by quantifying the florescence of DOX internalized by the cells after incubating for 3 hours. **Figure 14B** demonstrates the results of cellular uptake determined by measuring the florescence quantification, wherein free DOX showed highest florescence intensity amongst all the treatment group. The florescence intensity of DOX was found to be significantly ($p<0.01$) higher than 10µm-Sph particles and 10µm-SR particles. DOX-conjugated particles showed shape dependent impact on the cellular uptake with 10µm-sphere particles showing the minimal florescence intensity. The increase in aspect ratio led to increase in the florescence intensity with 10µm-SR particles showing ~1.2 folds increase as compared to 10µm-sphere particles. Similarly, 10µm-LR particles showed ~1.4 folds significant ($p<0.05$) increase in florescence intensity compared to spherical particles (**Figure 14B**).

These results are in accordance with the cellular uptake florescence imaging data indicating shape dependent effect of particles on uptake by SCLC cells wherein elongated particles are readily internalized compared to spherical particles. The increased uptake of DOX in the obtained results can be attributed to the gradient mediated passive diffusion while the DOX-conjugated particles undergo phagocytosis by the SCLC cells. These findings are in accordance to the previously published studies where microparticles with higher AR values are internalized faster by cancer cells [105,106].. Increase in the aspect ratio of conjugated particles resulted in increased uptake by cancer cells [105,107]. This can be because of increased fluidity of cancer cells' plasma membrane due to varied lipid metabolism resulting into improved uptake of the stretched particles (elongated with sharp ends) as against spherical particles unlike what was observed in the normal cells like

www.manaraa.com

macrophages [107–109]. These results confirmed that increase in aspect ratio of particles results into improved uptake of particles by SCLC cells.

4.8.2 Cytotoxicity assessment in SCLC cells

The cytotoxicity of free DOX and DOX-conjugated particles was evaluated by MTT assay after incubating H69AR cells for 72 hours over concentration range of 0.2 to 30 µM. Results as shown in **Figure 15A** indicate that free DOX has the highest cytotoxicity over the concentration range tested with an IC_{50} value of 8.3 ± 2.3 µM (**Figure 15B**). Treatment with 10µm-Sph showed a significant ($p<0.001$) ~2.6 folds reduction in the cytotoxicity against H69AR cells with an increased IC_{50} value of 21.6 ± 1.8 µM as compared to free DOX. Shape dependent effect was observed in the cytotoxicity of DOX-conjugated particles, wherein rod-shaped particles demonstrated better cytotoxicity against SCLC cells as compared to spherical particles. 10µm-SR particles showed improved cytotoxicity with reduced IC_{50} value of 18.1 ± 2.4 µM as against 10µm-Sph (**Figure 15A and 15B**). While treatment with 10µm-LR particles showed significant ($p<0.05$)1.4 folds reduction in IC_{50} value with 15.8 ± 2.5 µM as compared to 10µm-Sph particles, indicating superior cytotoxic effect against H69AR cells. These results are also supported by the cellular uptake results which infer that change in the shape of particles resulting into increased aspect ratio imparts improved cytotoxicity against SCLC cells. Blank particles cytotoxicity was also evaluated on H69AR cells after incubation for 72 hours. As can be seen in **Figure 15C**, all the three particles demonstrated >85% cell viability over the concentration range of 0.2 µM to 30 µM concentration. These results confirm that the blank particle are safe against H69AR cells and the cytotoxic effects observed is due to the DOX conjugated to the particles which was cleaved upon phagocytosis in the SCLC cells.

www.manaraa.com

(A)

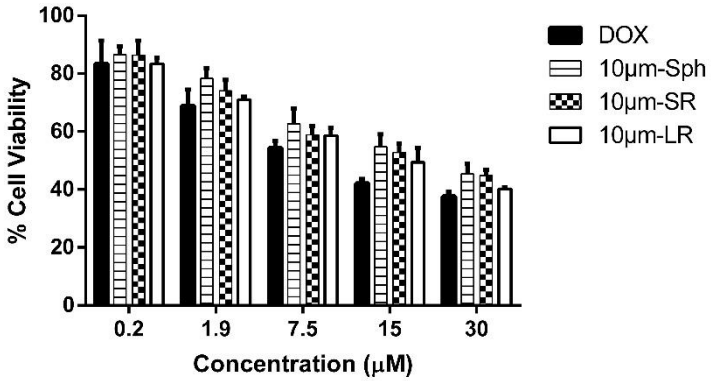

(B)

IC_{50} values in H69AR cells-72 hrs.	
Treatment groups	**IC_{50} Concentration (µM)**
DOX	8.3 ± 2.3
10 µm-Sph	21.6 ± 1.8
10 µm-SR	18.1 ± 2.4
10 µm-LR	15.8 ± 2.5

***
**
*
*

(C)

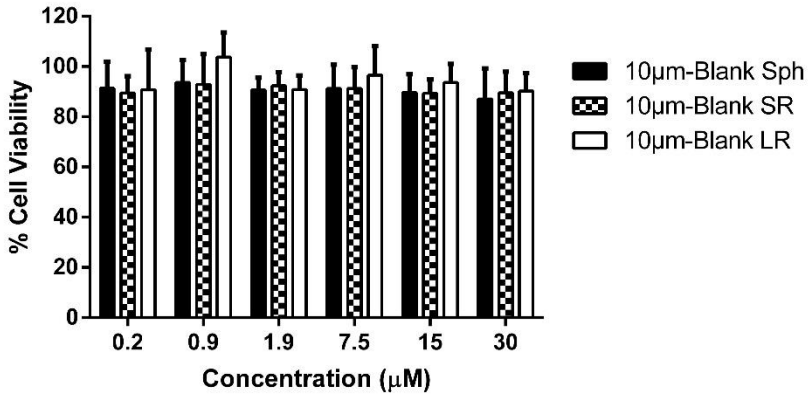

Figure 15: Cytotoxicity studies of various treatment groups after 72 hrs. incubation in H69AR cells. (A) Cytotoxic potential of DOX, and DOX-conjugated 10µm-Sph, 10µm-SR and 10µm-LR expressed as % cell viability. (B) IC50 values of DOX DOX and DOX conjugated particles calculated from the experimental cytotoxicity data (C) Cytotoxic potential of blank 10µm-Sph, 10µm-SR and 10µm-LR particles expressed as % cell viability. (Data represent mean ± SD of 3 individual experiments with n=6 for each experiment).

www.manaraa.com

4.8.3 In-vitro Tumor Simulation Studies

The monolayer cell culture studies (2D) does provide valuable information about the behavior of particles with cells; however, it does not truly reflect the *in-vivo* conditions. Therefore, to better assess the influence of particle shape in tumor conditions we performed *in-vitro* tumor simulation studies also known as 3D spheroid cell culture studies which simulates physiological tumorigenic conditions and provide relevant understanding about the therapeutic behavior of treatment as compared to the traditional monolayer studies [110,111]. 3D spheroid tumor models have been extensively explored in high throughput screening of lead compounds, evaluating the drug safety and efficacy profile, assessing the development of drug resistance and anti-tumorigenic activity of the delivery systems [112–114]. In this study, we have utilized in-vitro tumor simulation studies to evaluate the particle shape dependence on the anti-tumor activity of DOX-conjugated particles against H69AR SCLC cells. The study was performed at two different doses: 1) single dose study involves treatment to the cells only once at the start of experiments and 2) multiple dose- involves treatment at every 72 hours until the end of study. The anti-tumor efficacy of the treatment against the SCLC cells was measured in terms of spheroid volume, % cell viability in spheroids and imaging the live cells present in the spheroids using live-dead cell assay.

www.manaraa.com

(A)

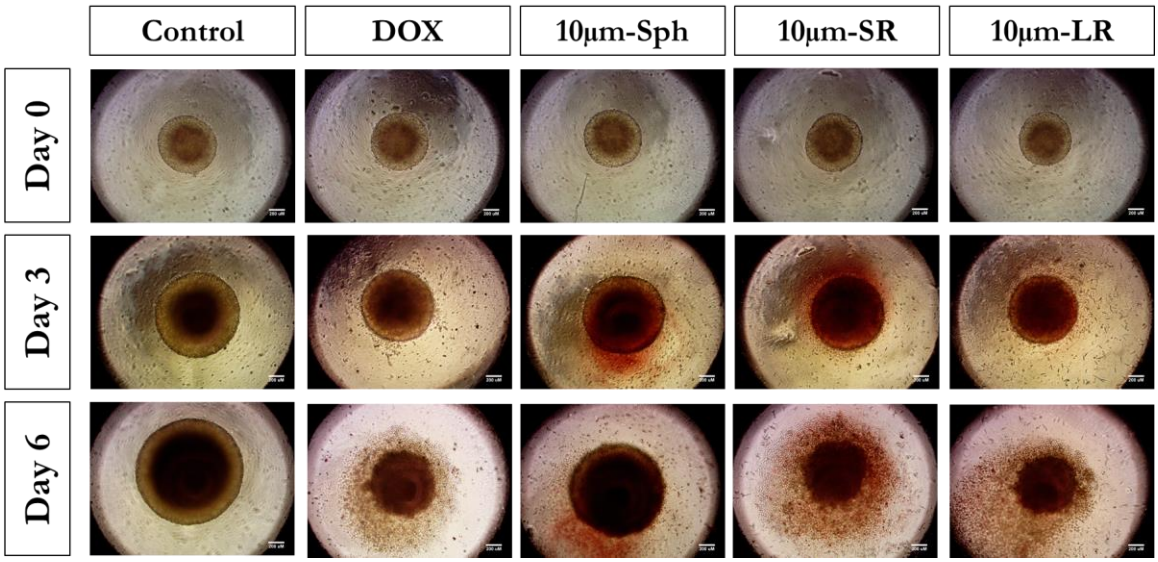

(B)

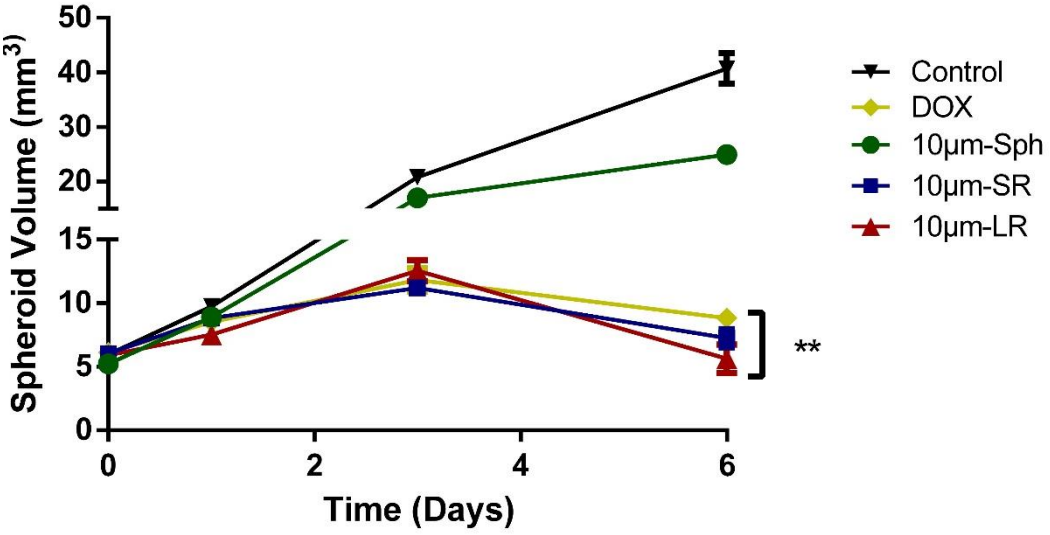

Figure 16: Effect of single dose treatment on tumorigenic activity of H69AR cells grown as 3D spheroids simulating in-vivo tumor conditions. (A) Representative images of spheroids demonstrating suppression in tumor growth at days 0, 3 and 6. Scale bar = 200 µm (B) Quantitative representation of anti-tumor activity of treatment expressed as spheroid volume (mm^3) versus time (days) for single dose treatment. Data represent mean±SEM (n = 6).

www.manaraa.com

A) In-vitro Tumor Simulation Studies- Single Dose

Figure 16A represents the tumor images of single dose treatment groups captured at different time intervals. As can be seen from the figure, control (untreated) group displayed uncontrolled tumor growth resulting into 40.7 ± 2.9 mm^3 volume of the spheroids at Day 6 (**Figure 16B**). Treatment with DOX and DOX-conjugated particles resulted into significant inhibition of tumor growth. DOX treatment resulted into inhibition in tumor growth along with loss of tumor integrity at Day 6 (**Figure 16A**) and a significant (p<0.001) 4.6 folds reduction in spheroid volume (8.8 ± 0.4 mm^3) as compared to control (**Figure 16B**). On the other hand, DOX-conjugated particles showed shape dependence anti-tumor effect against the H69AR spheroids wherein 10µm-Sph showed significant (p<0.001) 1.6 folds reduction in tumor growth as compared to control with tumor volume of 24.9 ± 0.5 mm^3 on day 6 and no influence on tumor integrity (**Figure 16A and 16B)**. While rod-shaped particles demonstrated superior tumor growth inhibition of SCLC spheroids as against spherical particles. 10µm-SR particles showed ~3.5 folds significant inhibition (p<0.001) of spheroid volume (7.2 ± 0.7 mm^3) and loss of tumor integrity at day 6 when compared to 10µm-Sph (**Figure 16A and 16B**). Treatment with 10µm-LR particles resulted into loss of tumor integrity and enhanced anti-tumor activity with spheroid volume of 5.6 ± 1.1 mm^3 showing ~4.4 folds and 1.6 folds reduction in spheroid volume when compared to 10µm-Sph (p<0.0001) and free DOX (p<0.05) respectively. These results signify the shape dependent impact of particles on the anti-tumorigenic activity of DOX against H69AR tumors with LR particles demonstrating the highest tumor growth inhibition amongst all the treatment groups.

www.manaraa.com

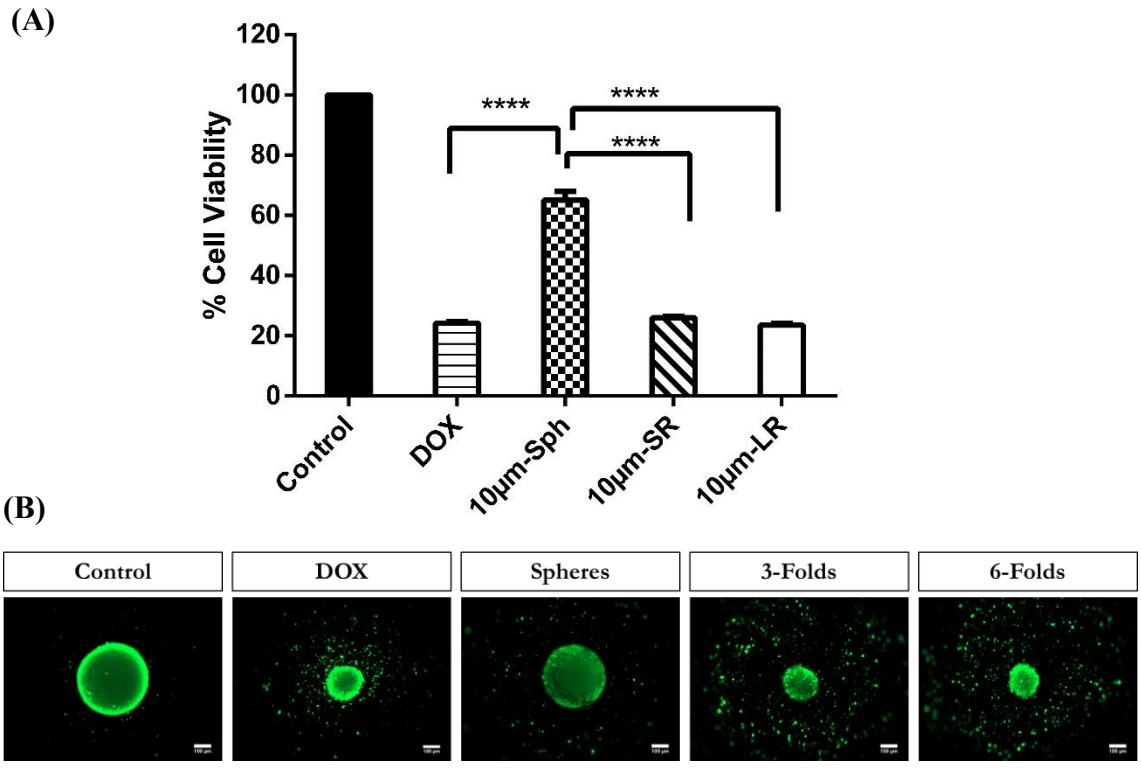

Figure 17: Effect of single dose treatment on tumorigenic activity of H69AR cells grown as 3D spheroids simulating in-vivo tumor conditions. (A) % Cell viability of spheroids obtained using Cell-titer glo™ 3D calculated relative to untreated cells (control) considered as 100%. Data represents mean±SD (n=3). (B) Representative florescent images of spheroids after staining the live cells with calcein AM dye at the end of day 6. ****p<0.0001.

The 3D spheroids model represent a solid mass of tumor cells growing exponentially in all the direction and therefore, optical imaging may not completely reflect treatment's efficiency. Therefore, % cell viability in 3D spheroids was performed to determine % viable cells present in the tumor after the treatment period. **Figure 17C** represents the % cell viability of 3D spheroids for each treatment group, wherein DOX shows 24.2 ± 2.0 % viability in spheroids after 6 days. Treatment with 10µm-Sph, demonstrated 65.1 ± 4.4 % viability while the stretched particles demonstrated significantly

www.manaraa.com

(p<0.0001) lower cell viability with 26.0 ± 2.1 % viability for 10µm-SR and 23.5 ± 3.1 % viability for 10µm-LR (**Figure 17C**). These results indicate that treatment with the stretched particles results into evident reduction in % viability compared to the spherical particles. This data is also in accordance with the optical imaging data and tumor spheroid volume establishing the particle shape effects against the 3D spheroids tumorigenic activity.

To further validate the effectiveness of treatment groups against SCLC spheroids, live cells present in the spheroids were imaged after staining with calcein AM dye (providing green florescence). **Figure 17D** displays the florescent images of viable cells in 3D spheroids present in each treatment group. As can be inferred from the figure, control has intense bright green florescence indicating the presence of live cells. Further, treatment with DOX resulted into inhibition of the tumor growth when compared to control with reduced viable cells being present in the spheroids. For 10µm-Sph, even though the size of the spheroids was not significantly reduced, the florescence of the viable cells was diminished (**Figure 17D**). This can be suggestive of the fact that 10µm-Sph may be able to show cytotoxic effects without impacting the tumor size and the integrity of the spheroids, however this effect was non-significant. On the contrary, treatment with rod-shaped particles (10µm-SR and 10µm-LR) resulted into reduction in tumor size as well as diminished florescence of viable cells compared to spherical particles indicating their superior anti-tumorigenic activity (**Figure 17D)**. These results are indicative of the fact that particle shape does influence the tumorigenic action of H69AR cells in the *in-vitro* simulation studies.

www.manaraa.com

(A)

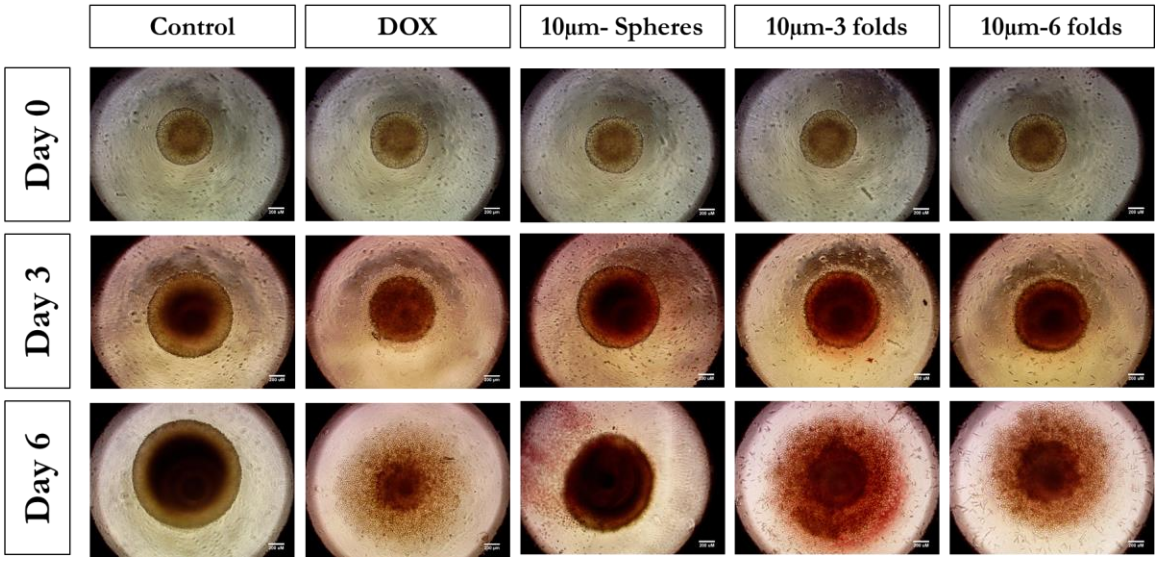

(B)

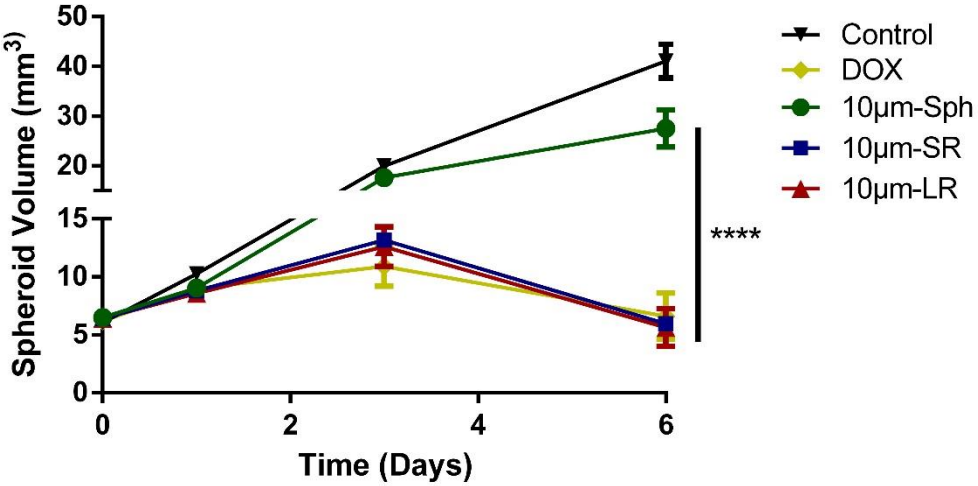

Figure 18: Effect of multiple dose treatment on tumorigenic activity of H69AR cells grown as 3D spheroids simulating in-vivo tumor conditions. (A) Representative images of spheroids demonstrating suppression in tumor growth at days 0, 3 and 6. Scale bar = 200 µm (B) Quantitative representation of anti-tumor activity of treatment expressed as spheroid volume (mm^3) versus time (days) for multiple dose treatment. Data represent mean±SEM (n = 6).

www.manaraa.com

B) In-vitro Tumor Simulation Studies- Multiple Dose

Multiple dose treatment revealed interesting results establishing the anti-tumor activity of various treatment groups. As seen in **Figure 18A**, the control group demonstrated 6.8 folds significant increase ($p<0.001$) in the tumor growth with 41.1 ± 3.4 mm^3 spheroid volume at day 6 when compared to the initial (day 0) tumor volume (**Figure 18B)**. DOX treatment resulted into inhibition of tumor growth and a significant ($p<0.0001$) 6.2 folds reduction in spheroid volume (6.6 ± 2.2 mm^3) as compared to control (**Figure 18B**). Additionally, DOX also resulted into distortion of tumor integrity at Day 6 which is a characteristic anti-tumorigenic activity of chemotherapeutic agent (**Figure 18A)**. Treatment with DOX-conjugated particles demonstrated the influence of particle shape on the treatment effectiveness. 10µm-Sph demonstrated significant ($p<0.001$) reduction of 1.5 folds in spheroid volume with 27.5 ± 3.7 mm^3 when compared to control. This effect was found to be more pronounced with treatment of rod-shaped particles 10µm-SR particles demonstrated a significant ($p<0.0001$) 7.0 folds reduction in spheroid growth with a tumor volume of 5.9 ± 0.5 mm^3 as against control and ~5.0 folds reduction when compared to spherical particles (**Figure 18A and 18B**). Treatment with 10µm-LR particles resulted into 5.6 ± 1.1 mm^3 spheroid volume as in **Figure 18B** demonstrating a significant ($p<0.0001$) 5.0 folds reduction as against 10µm-Sph. In addition to reduction in tumor growth and spheroid volume, it was interesting to observe that the rod-shaped particles impacted the tumor integrity which was found to be absent in the spherical particles . These results may be suggestive of the fact that rod-shaped particles possess better anti-tumorigenic activity against H69AR cells when compared to spherical particles.

www.manaraa.com

(A)

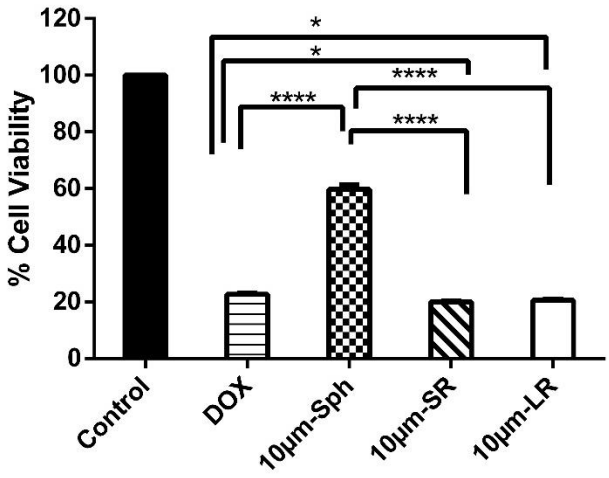

(B)

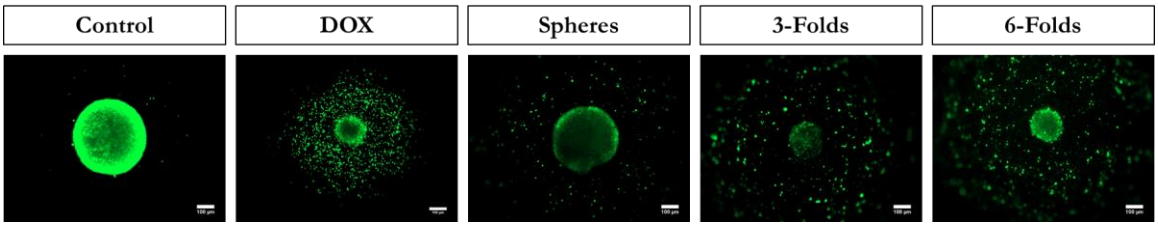

Figure 19: Effect of multiple dose treatment on tumorigenic activity of H69AR cells grown as 3D spheroids simulating in-vivo tumor conditions. (A) % Cell viability of spheroids obtained using Cell-titer Glo™ 3D calculated relative to untreated cells (control) considered as 100%. Data represents mean±SD (n=3). (B) Representative florescent images of spheroids after staining the live cells with calcein AM dye at the end of day 6. *p<0.05 and ****p<0.0001.

% Cell viability of 3D spheroids for each treatment group was analyzed using luminescence to further support the data of microscopic imaging. As seen in **Figure 19A**, DOX demonstrated 22.7 ± 1.7% cell viability after 6 days. Upon evaluating DOX-conjugated particles, shape dependent effect was predominantly observed with spherical particles demonstrating the lowest % viability with 59.7 ± 2.5 % while rod-shaped particles resulted into significant (p<0.0001) 3 folds reduction in viability with ~20 % cell viability.

www.manaraa.com

Furthermore, treatment with 10µm-SR and 10µm-LR particles also resulted into significant (p<0.05) reduction in % cell viability as compared to free DOX. These results are in accordance with the tumor imaging and spheroids volume data signifying the importance of particle shape in improving the efficacy of treatment.

The viable cells in the 3D spheroids were stained with calcein AM dye, to understand the therapeutic behavior of treatment groups by imaging the viable cells and further validate the microscopic and luminescence data. As seen in the **Figure 19B**, control group displays bright green florescence indicating the presence of viable cells. Treatment with DOX resulted into reduction in the tumor size and the viable cells florescence as compared to control. Particle shape dependent effect on tumorigenic activity of H69AR spheroids was analyzed using 10µm-Sph, 10µm-SR, and 10µm-LR particles. The spherical particles indicated minimal reduction in the tumor size amongst the conjugated DOX particles (**Figure 19B)**. However, the florescence of viable cells in the 10µm-Sph treatment was found to be diminished indicating that the spherical particles does show cytotoxicity without impacting the tumor integrity. Treatment with both the rod-shaped particles demonstrated reduction in tumor size unlike the spherical particles. Additionally, the florescence of the viable cells in both the groups was found to be diminished compared to free DOX treated spheroids (**Figure 19B)**. These findings indicate the pronounced effectiveness of the particles upon changing the shape from spherical to rod-shape, thereby imparting better therapeutic activity.

The results of *in-vitro* tumor simulation studies establish the superior anti-tumorigenic activity of rod-shaped particles against spheres which may be suggestive of better penetrability of rod-shaped particles in the 3D spheroids. However, increase in AR

www.manaraa.com

of rod-shaped particles did not significantly influence the penetrability in the spheroids as can be seen for SR and LR which are in accordance with previously reported studies [115,116]. Studies performed by Chauhan *et al*., demonstrated 1.7 folds improvement in penetration of nanorods against spherical counterparts evaluated in orthotopic E0771 mammary tumors. Similarly, Black *et al*., performed *in-vivo* studies to evaluate the efficacy of various particle shape of radiolabeled silver nanoparticles (rods, disks, spheres, and cube)in penetrating the solid tumor upon intravenous administration. It was reported that rods and cube shaped particles penetrated to the core of tumor while the disk- and sphere-shaped particles were predominantly located at the rim of the tumor [117]. These studies have reported the internalization of nanosized particles which may be internalized via mechanisms such as diffusion, endocytosis, or pinocytosis while the particles used in our project are micron-sized which are extensively internalized via phagocytosis wherein again the influence of shape has been severely signified [60,118]. The results of *in-vitro* tumor simulation therefore establish the improved effectiveness of treatment by change of particle shape form sphere to rod-shape.

4.9 Investigating Impact on Cardiotoxicity

Therapeutic use of DOX has been limited owing to its adverse side effects amongst which deposition of cumulative dose causes cardiotoxicity [119]. Clinically induced DOX cardiotoxicity leads to development of cardiomyopathy subsequently causing apoptosis and necrosis of cardiomyocytes leading to progressive cardiac failure [120]. Several mechanisms have been identified for development of DOX induced cardiotoxicity such as reactive oxygen species production, apoptosis, DNA damage, lipid peroxidation and autophagy [69]. As particle shape has shown to influence the internalization of particles in

www.manaraa.com

normal cells like macrophages, with minimal uptake of high AR particles, we hypothesized that conjugation of DOX to rod shaped particles may result into reduced cardiotoxic activity of DOX due to reduced uptake.

4.9.1 Cytotoxic Assessment on Cardiomyoblasts

The viability of H9c2 rat cardiomyoblasts cells was analyzed using MTT assay after 24 hours of exposure to various treatment groups as shown in **Figure 20A**. As seen from the figure, DOX displayed dose dependent toxicity against H9c2 cells and the IC_{50} value of DOX was found to be 37.1 ± 3.0 µM which is in accordance with the IC_{50} value reported in literature. Treatment with 10µm-Sph displayed 1.6 folds reduction *(p*<0.001) in cytotoxicity as compared to free DOX with 61.1 ± 7.2 % cell viability observed at 40 µM concentration, the highest concentration tested. Both the rod-shaped particles, 10µm-SR and 10µm-LR also demonstrated a significant (p<0.0001) reduction in the cytotoxicity as compared to the free DOX (**Figure 20A**). The % cell viability after treatment with 10µm-SR particles was found to be 78.0 ±9.3 % cell viability while 10µm-LR particles showed 80.3 ± 6.1 % cell viability at 40 µM concentration. These results clearly show that DOX-conjugated particles resulted into lower cytotoxic effects against H9c2 cells. Amongst the DOX-conjugated particles, change in the shape of particle to rod-shape further resulted into lower cytotoxicity as compared to the spherical particles.

www.manaraa.com

(A)

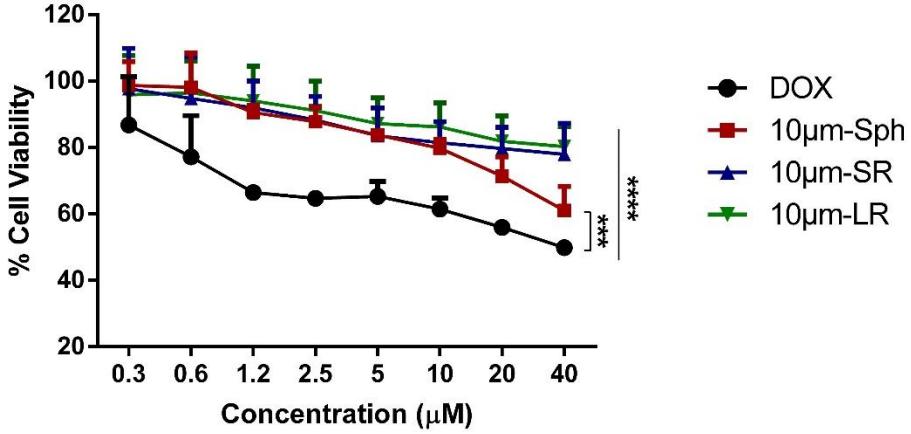

(B)

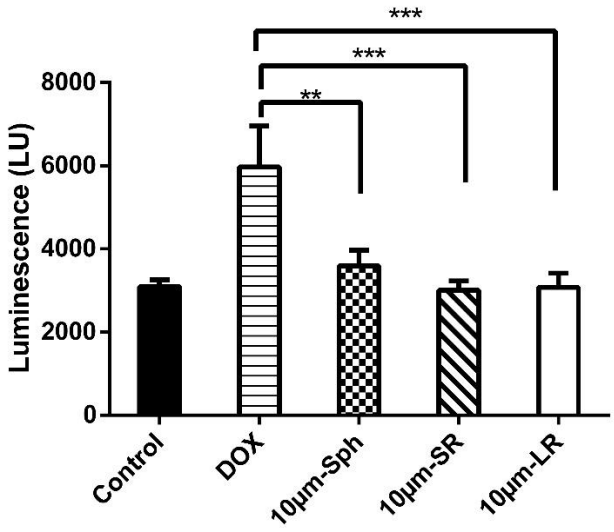

(C)

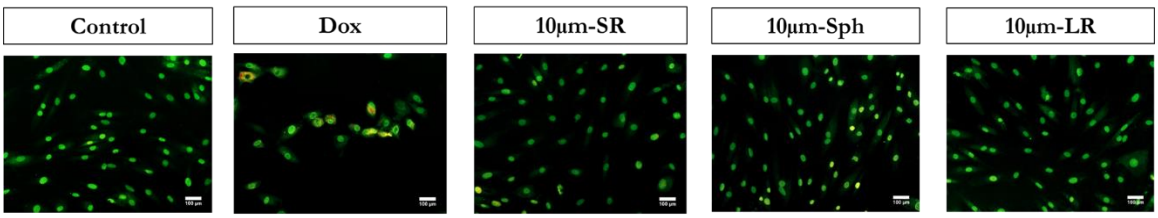

Figure 20: Influence of cardiotoxicity of DOX and DOX-conjugated particles after treatment of H9c2 cardiomyoblasts. (A) Cytotoxic potential of treatment groups evaluated after 24 hrs. treatments and expressed as % cell viability (n=6 for 3 individual experiments). (B) Apoptosis effect of free DOX and DOX-conjugated particles evaluated using Realtime-Glo™ expressed as luminescence intensity (n=6) and (C) Representative florescence images of H9c2 cardiomyoblasts stained by AO/EB staining. Data represents mean±SD. ** $p<0.01$ and *** $p<0.001$.

www.manaraa.com

4.9.2 Lactate Dehydrogenase (LDH) Assay

LDH is a cytosolic enzyme released upon damage to the cell membrane and is well known marker of cell death or cell damage. Cell injury to H9c2 cardiomyoblasts after treatment for 24 hours was evaluated by measuring the LDH release in the media using the Promega Luminescence kit. As seen in **Figure 20B** free DOX (1.25 µM) induces the highest increase in the luminescence signal amongst all the treatment groups suggesting significant (p<0.001) LDH leakage in cell culture supernatant following 24 hours incubation. Therefore, indicating that exposure to free DOX resulted in significant damage to cell membrane. However, treatment with DOX-conjugated 10µm-Sph particles displayed a significant (p<0.01) reduction in the LDH release from H9c2 cells. Furthermore, incubation of cardiomyoblasts with rod-shaped particles i.e., 10µm-SR and 10µm-LR resulted into 2.0 folds significant (p<0.001) reduction in the LDH activity as compared to free DOX (**Figure 20B**). The LDH activity of the DOX-conjugated particles were almost like the control indicating the role of microparticles in reducing the cardiotoxicity of free DOX. This can be attributed to the conjugation of DOX to polystyrene particles via a stable amide linkage which prevents DOX to be readily available. The small increase in LDH activity observed for 10µm-Sph compared to 10µm-SR and 10µm-LR particles may be because of preferential internalization of spherical particles against the rod-shaped particles like macrophages.

www.manaraa.com

4.9.3 Apoptosis Evaluation in H9c2 cells

Several *in-vitro* and *in-vivo* studies have reported that DOX induces apoptosis in the cardiomyocytes, thereby indicating that apoptosis is major pathway leading to cardiac dysfunction and eventually cardiac failure in patients. **Figure 20C** demonstrates the effect of free DOX and DOX-conjugated particles on the apoptosis induced damage in H9c2 cardiomyocytes using acridine orange (AO)/ethidium bromide (EB) staining. Ethidium bromide enters the cell with compromised cell membrane integrity and stains the cells with red or orange fluorescence indicating the induction of apoptosis eventually causing cell death. The results demonstrate that exposure of cells to free DOX resulted into reduced cell viability and staining of the cells with red color indicating the presence of non-viable cells [69]. Treatment with all the DOX-conjugated particles showed absence of red/orange-stained cells indicating absence of cytotoxic effects on the H9c2 cardiomyocytes (**Figure 20C**). These results are in corroboration with the cytotoxicity and LDH activity assay further confirming the diminished activity of DOX upon being conjugated to the polystyrene particles.

www.manaraa.com

5.0 Conclusion

In this project we demonstrated the interplay between the particle size and particle shape on the aerodynamic properties using NGI. Our results showed that change in the particle shape from spherical to rod-shaped display improved aerodynamic behavior of particles and this effect was amplified amongst particles with large equivalent diameter. Subsequently, we have assessed the influence of particle shape on escape of phagocytic uptake by macrophages wherein rod-shape particles displayed reduced uptake compared to spherical particles and this effect being higher for elongated particles having higher AR value. The current study also provides evidence about particle shape influence on the effectiveness of treatment against SCLC cells. Results demonstrated superior cytotoxic activity of rod-shaped particles against spherical particles. Importantly, these results were further validated using *in-vitro* tumor simulation studies wherein the rod-shaped particles have pronounced effect in inhibiting the tumor growth and distorting the tumor integrity which would help translation to preclinical settings. Furthermore, we have evaluated the particle shape effect on cardiotoxicity of DOX using DOX-conjugated in cardiomyoblasts. Results confirmed that elongated rod-shaped particles illustrated diminished cardiotoxicity on cells when compared to their spherical counterparts. Therefore, our findings provide valuable insights about particle shape influence on designing inhalable delivery carriers for pulmonary administration to combat respiratory diseases.

Since this proof-of-concept study was performed using polystyrene particles which are non-biodegradable, the translation to preclinical setting remains challenging. Therefore, future studies may involve developing biodegradable particles of various shapes and evaluate their impact on pulmonary deposition behavior. Moreover, the existing rod-

www.manaraa.com

shaped particles can be conjugated with other small molecules or large molecules such as targeting proteins. This strategy can be further translated to fabricate other biodegradable rod-shaped particles with tunable surface modifications for providing desired therapeutic effects. The biodegradable particles can be conjugated with variety of therapeutics or can be passively loaded with drug molecules of interest. *In-vivo* studies can be performed in orthotopic lung tumor model to further validate the influence of particle shape on the aerosolization efficiency and the therapeutic activity, thereby designing optimized delivery carriers for pulmonary drug delivery.

www.manaraa.com

6.0 References

[1] Definition of respiratory disease - NCI Dictionary of Cancer Terms - National Cancer Institute, (2011). https://www.cancer.gov/publications/dictionaries/cancer-terms/def/respiratory-disease (accessed January 10, 2021).

[2] The top 10 causes of death, (n.d.). https://www.who.int/news-room/fact-sheets/detail/the-top-10-causes-of-death (accessed March 12, 2019).

[3] D.A. Groneberg, C. Witt, U. Wagner, K.F. Chung, A. Fischer, Fundamentals of pulmonary drug delivery, Respiratory Medicine. 97 (2003) 382–387. https://doi.org/10.1053/rmed.2002.1457.

[4] N.R. Labiris, M.B. Dolovich, Pulmonary drug delivery. Part I: Physiological factors affecting therapeutic effectiveness of aerosolized medications, Br J Clin Pharmacol. 56 (2003) 588–599. https://doi.org/10.1046/j.1365-2125.2003.01892.x.

[5] J.M. Borghardt, C. Kloft, A. Sharma, Inhaled Therapy in Respiratory Disease: The Complex Interplay of Pulmonary Kinetic Processes, Canadian Respiratory Journal. 2018 (2018) e2732017. https://doi.org/10.1155/2018/2732017.

[6] J.L. Rau, The inhalation of drugs: advantages and problems, Respir Care. 50 (2005) 367–382.

[7] A.M. Le Roux, D. Kotze, C.A. Wium, P.P. Van Jaarsveld, J.R. Joubert, Inhaled and oral salbutamol: how effective in the prophylaxis of asthma?, Respiration. 58 (1991) 192–197. https://doi.org/10.1159/000195925.

[8] A. Dyreborg, N. Krogh, V. Backer, S. Rzeppa, P. Hemmersbach, M. Hostrup, Pharmacokinetics of Oral and Inhaled Terbutaline after Exercise in Trained Men, Front Pharmacol. 7 (2016). https://doi.org/10.3389/fphar.2016.00150.

www.manaraa.com

[9] J.G.Y. Chan, J. Wong, Q.T. Zhou, S.S.Y. Leung, H.-K. Chan, Advances in Device and Formulation Technologies for Pulmonary Drug Delivery, AAPS PharmSciTech. 15 (2014) 882–897. https://doi.org/10.1208/s12249-014-0114-y.

[10] M. Shirley, Amikacin Liposome Inhalation Suspension: A Review in Mycobacterium avium Complex Lung Disease, Drugs. 79 (2019) 555–562. https://doi.org/10.1007/s40265-019-01095-z.

[11] D.A. Edwards, Large Porous Particles for Pulmonary Drug Delivery, Science. 276 (1997) 1868–1872. https://doi.org/10.1126/science.276.5320.1868.

[12] I.M. El-Sherbiny, N.M. El-Baz, M.H. Yacoub, Inhaled nano- and microparticles for drug delivery, Global Cardiology Science and Practice. 2015 (2015) 2. https://doi.org/10.5339/gcsp.2015.2.

[13] A.Y. Watson, R.R. Bates, D. Kennedy, Biological Disposition of Airborne Particles: Basic Principles and Application to Vehicular Emissions, National Academies Press (US), 1988. https://www.ncbi.nlm.nih.gov/books/NBK218161/ (accessed September 12, 2020).

[14] S.G. Klein, J. Hennen, T. Serchi, B. Blömeke, A.C. Gutleb, Potential of coculture in vitro models to study inflammatory and sensitizing effects of particles on the lung, Toxicology in Vitro. 25 (2011) 1516–1534. https://doi.org/10.1016/j.tiv.2011.09.006.

[15] K.P. O'Donnell, H.D.C. Smyth, Macro- and Microstructure of the Airways for Drug Delivery, in: H.D.C. Smyth, A.J. Hickey (Eds.), Controlled Pulmonary Drug Delivery, Springer, New York, NY, 2011: pp. 1–19. https://doi.org/10.1007/978-1-4419-9745-6_1.

www.manaraa.com

[16] M. Ochs, J.R. Nyengaard, A. Jung, L. Knudsen, M. Voigt, T. Wahlers, J. Richter, H.J.G. Gundersen, The Number of Alveoli in the Human Lung, Am J Respir Crit Care Med. 169 (2004) 120–124. https://doi.org/10.1164/rccm.200308-1107OC.

[17] J.S. Patil, S. Sarasija, Pulmonary drug delivery strategies: A concise, systematic review, Lung India. 29 (2012) 44–49. https://doi.org/10.4103/0970-2113.92361.

[18] S. Toppila-Salmi, J. Renkonen, S. Joenväärä, P. Mattila, R. Renkonen, Allergen interactions with epithelium, Current Opinion in Allergy and Clinical Immunology. 11 (2011) 29–32. https://doi.org/10.1097/ACI.0b013e328342319e.

[19] T.J. Franks, T.V. Colby, W.D. Travis, R.M. Tuder, H.Y. Reynolds, A.R. Brody, W.V. Cardoso, R.G. Crystal, C.J. Drake, J. Engelhardt, M. Frid, E. Herzog, R. Mason, S.H. Phan, S.H. Randell, M.C. Rose, T. Stevens, J. Serge, M.E. Sunday, J.A. Voynow, B.M. Weinstein, J. Whitsett, M.C. Williams, Resident Cellular Components of the Human Lung, Proc Am Thorac Soc. 5 (2008) 763–766. https://doi.org/10.1513/pats.200803-025HR.

[20] M.M. Chang, L. Shih, R. Wu, 1 Pulmonary Epithelium: Cell Types and Functions, n.d.

[21] B.S. Schuster, J.S. Suk, G.F. Woodworth, J. Hanes, Nanoparticle diffusion in respiratory mucus from humans without lung disease, Biomaterials. 34 (2013) 3439–3446. https://doi.org/10.1016/j.biomaterials.2013.01.064.

[22] D.T. Edizer, O. Yigit, M. Rudenko, Mucociliary Clearance and Its Importance, in: C. Cingi, N. Bayar Muluk (Eds.), All Around the Nose: Basic Science, Diseases and Surgical Management, Springer International Publishing, Cham, 2020: pp. 65–70. https://doi.org/10.1007/978-3-030-21217-9_7.

www.manaraa.com

[23] J.V. Fahy, B.F. Dickey, Airway mucus function and dysfunction, N. Engl. J. Med. 363 (2010) 2233–2247. https://doi.org/10.1056/NEJMra0910061.

[24] F. Taherali, F. Varum, A.W. Basit, A slippery slope: On the origin, role and physiology of mucus, Advanced Drug Delivery Reviews. 124 (2018) 16–33. https://doi.org/10.1016/j.addr.2017.10.014.

[25] J.A. Frank, Claudins and alveolar epithelial barrier function in the lung, Ann N Y Acad Sci. 1257 (2012) 175–183. https://doi.org/10.1111/j.1749-6632.2012.06533.x.

[26] C.A. Ruge, J. Kirch, O. Cañadas, M. Schneider, J. Perez-Gil, U.F. Schaefer, C. Casals, C.-M. Lehr, Uptake of nanoparticles by alveolar macrophages is triggered by surfactant protein A, Nanomedicine. 7 (2011) 690–693. https://doi.org/10.1016/j.nano.2011.07.009.

[27] T. Tschernig, N.T. Veith, E. Diler, M. Bischoff, C. Meier, M. Schicht, The importance of surfactant proteins—New aspects on macrophage phagocytosis, Annals of Anatomy - Anatomischer Anzeiger. 208 (2016) 142–145. https://doi.org/10.1016/j.aanat.2016.07.005.

[28] R. Guagliardo, J. Pérez-Gil, S. De Smedt, K. Raemdonck, Pulmonary surfactant and drug delivery: Focusing on the role of surfactant proteins, Journal of Controlled Release. 291 (2018) 116–126. https://doi.org/10.1016/j.jconrel.2018.10.012.

[29] S. Ariki, C. Nishitani, Y. Kuroki, Diverse Functions of Pulmonary Collectins in Host Defense of the Lung, Journal of Biomedicine and Biotechnology. 2012 (2012) e532071. https://doi.org/10.1155/2012/532071.

www.manaraa.com

[30] J.A. Whitsett, T.E. Weaver, Hydrophobic Surfactant Proteins in Lung Function and Disease, New England Journal of Medicine. 347 (2002) 2141–2148. https://doi.org/10.1056/NEJMra022387.

[31] K. BéruBé, Z. Prytherch, C. Job, T. Hughes, Human primary bronchial lung cell constructs: The new respiratory models, Toxicology. 278 (2010) 311–318. https://doi.org/10.1016/j.tox.2010.04.004.

[32] C.A. Ruge, J. Kirch, C.-M. Lehr, Pulmonary drug delivery: from generating aerosols to overcoming biological barriers—therapeutic possibilities and technological challenges, The Lancet Respiratory Medicine. 1 (2013) 402–413. https://doi.org/10.1016/S2213-2600(13)70072-9.

[33] J. Heyder, Deposition of Inhaled Particles in the Human Respiratory Tract and Consequences for Regional Targeting in Respiratory Drug Delivery, Proceedings of the American Thoracic Society. 1 (2004) 315–320. https://doi.org/10.1513/pats.200409-046TA.

[34] M. Lippmann, D.B. Yeates, R.E. Albert, Deposition, retention, and clearance of inhaled particles., Br J Ind Med. 37 (1980) 337–362.

[35] C. Darquenne, Aerosol Deposition in Health and Disease, J Aerosol Med Pulm Drug Deliv. 25 (2012) 140–147. https://doi.org/10.1089/jamp.2011.0916.

[36] C. Darquenne, Deposition Mechanisms, Journal of Aerosol Medicine and Pulmonary Drug Delivery. 33 (2020) 181–185. https://doi.org/10.1089/jamp.2020.29029.cd.

www.manaraa.com

[37] A. Tsuda, F.S. Henry, J.P. Butler, Particle Transport and Deposition: Basic Physics of Particle Kinetics, in: Comprehensive Physiology, American Cancer Society, 2013: pp. 1437–1471. https://doi.org/10.1002/cphy.c100085.

[38] Y.S. Cheng, Aerosol Deposition in the Extrathoracic Region, Aerosol Science and Technology. 37 (2003) 659–671. https://doi.org/10.1080/02786820300906.

[39] T.S. Wiedmann, R. Bhatia, L.W. Wattenberg, Drug solubilization in lung surfactant, Journal of Controlled Release. 65 (2000) 43–47. https://doi.org/10.1016/S0168-3659(99)00230-8.

[40] G. Oberdörster, Lung Clearance of Inhaled Insoluble and Soluble Particles, Journal of Aerosol Medicine. 1 (1988) 289–330. https://doi.org/10.1089/jam.1988.1.289.

[41] H. Nakane, Translocation of particles deposited in the respiratory system: a systematic review and statistical analysis, Environ Health Prev Med. 17 (2012) 263–274. https://doi.org/10.1007/s12199-011-0252-8.

[42] H.S. Choi, Y. Ashitate, J.H. Lee, S.H. Kim, A. Matsui, N. Insin, M.G. Bawendi, M. Semmler-Behnke, J.V. Frangioni, A. Tsuda, Rapid Translocation of Nanoparticles from the Lung Airspaces to the Body, Nat Biotechnol. 28 (2010) 1300–1303. https://doi.org/10.1038/nbt.1696.

[43] Y. Liu, A. Ibricevic-Richardson, J.A. Cohen, J.L. Cohen, S.P. Gunsten, J.M.J. Fréchet, M.J. Walter, M.J. Welch, S.L. Brody, Impact of hydrogel nanoparticle size and functionalization on in vivo behavior for lung imaging and therapeutics, Mol Pharm. 6 (2009) 1891–1902. https://doi.org/10.1021/mp900215p.

[44] A. Buckley, J. Warren, A. Hodgson, T. Marczylo, K. Ignatyev, C. Guo, R. Smith, Slow lung clearance and limited translocation of four sizes of inhaled iridium

www.manaraa.com

nanoparticles, Particle and Fibre Toxicology. 14 (2017) 5. https://doi.org/10.1186/s12989-017-0185-5.

[45] C.M. Evans, J.S. Koo, Airway mucus: the good, the bad, the sticky, Pharmacol. Ther. 121 (2009) 332–348. https://doi.org/10.1016/j.pharmthera.2008.11.001.

[46] S. Schürch, P. Gehr, V. Im Hof, M. Geiser, F. Green, Surfactant displaces particles toward the epithelium in airways and alveoli, Respir Physiol. 80 (1990) 17–32. https://doi.org/10.1016/0034-5687(90)90003-h.

[47] W. Stahlhofen, R. Koebrich, G. Rudolf, G. Scheuch, Short-term and long-term clearance of particles from the upper human respiratory tract as function of particle size, Journal of Aerosol Science. 21 (1990) S407–S410. https://doi.org/10.1016/0021-8502(90)90267-2.

[48] G. Scheuch, W. Stahlhofen, Particle Deposition of Inhaled Aerosol Boluses in the Upper Human Airways, Journal of Aerosol Medicine. 1 (1988) 29–36. https://doi.org/10.1089/jam.1988.1.29.

[49] J.R.H. Smith, M.R. Bailey, G. Etherington, A.L. Shutt, M.J. Youngman, Effect of Particle Size on Slow Particle Clearance from the Bronchial Tree, Experimental Lung Research. 34 (2008) 287–312. https://doi.org/10.1080/01902140802093196.

[50] A. Henning, M. Schneider, N. Nafee, L. Muijs, E. Rytting, X. Wang, T. Kissel, D. Grafahrend, D. Klee, C.-M. Lehr, Influence of Particle Size and Material Properties on Mucociliary Clearance from the Airways, Journal of Aerosol Medicine and Pulmonary Drug Delivery. 23 (2010) 233–241. https://doi.org/10.1089/jamp.2009.0806.

www.manaraa.com

[51] J.C. Hogg, Response of the lung to inhaled particles, Medical Journal of Australia. 142 (1985) 675–678. https://doi.org/10.5694/j.1326-5377.1985.tb113589.x.

[52] M. Geiser, Update on Macrophage Clearance of Inhaled Micro- and Nanoparticles, Journal of Aerosol Medicine and Pulmonary Drug Delivery. 23 (2010) 207–217. https://doi.org/10.1089/jamp.2009.0797.

[53] P.G. Holt, D.H. Strickland, M.E. Wikström, F.L. Jahnsen, Regulation of immunological homeostasis in the respiratory tract, Nature Reviews Immunology. 8 (2008) 142–152. https://doi.org/10.1038/nri2236.

[54] D.M. Ward, D.P. Hackenyos, J. Kaplan, Fusion of sequentially internalized vesicles in alveolar macrophages., J Cell Biol. 110 (1990) 1013–1022. https://doi.org/10.1083/jcb.110.4.1013.

[55] B. Patel, N. Gupta, F. Ahsan, Particle engineering to enhance or lessen particle uptake by alveolar macrophages and to influence the therapeutic outcome, European Journal of Pharmaceutics and Biopharmaceutics. 89 (2015) 163–174. https://doi.org/10.1016/j.ejpb.2014.12.001.

[56] J.V. Castell, M. Teresa Donato, M.J. Gómez-Lechón, Metabolism and bioactivation of toxicants in the lung. The in vitro cellular approach, Experimental and Toxicologic Pathology. 57 (2005) 189–204. https://doi.org/10.1016/j.etp.2005.05.008.

[57] R. Upton, D. Doolette, Kinetic Aspects of Drug Disposition in the Lungs, Clinical and Experimental Pharmacology and Physiology. 26 (1999) 381–391. https://doi.org/10.1046/j.1440-1681.1999.03048.x.

المنارة للاستشارات
www.manaraa.com

[58] M. Gabriele, P. Puccini, M. Lucchi, A. Vizziello, P.G. Gervasi, V. Longo, Presence and inter-individual variability of carboxylesterases (CES1 and CES2) in human lung, Biochemical Pharmacology. 150 (2018) 64–71. https://doi.org/10.1016/j.bcp.2018.01.028.

[59] S. Chakraborti, J. Sarkar, P.K. Pramanik, T. Chakraborti, Role of Proteases in Lung Disease: A Brief Overview, in: S. Chakraborti, T. Chakraborti, N.S. Dhalla (Eds.), Proteases in Human Diseases, Springer, Singapore, 2017: pp. 333–374. https://doi.org/10.1007/978-981-10-3162-5_16.

[60] J.A. Champion, S. Mitragotri, Shape Induced Inhibition of Phagocytosis of Polymer Particles, Pharm Res. 26 (2009) 244–249. https://doi.org/10.1007/s11095-008-9626-z.

[61] J.A. Champion, S. Mitragotri, Role of target geometry in phagocytosis, PNAS. 103 (2006) 4930–4934. https://doi.org/10.1073/pnas.0600997103.

[62] R.S. Elbatanony, V. Parvathaneni, N.S. Kulkarni, S.K. Shukla, G. Chauhan, N.K. Kunda, V. Gupta, Afatinib-loaded inhalable PLGA nanoparticles for localized therapy of non-small cell lung cancer (NSCLC)—development and in-vitro efficacy, Drug Deliv. and Transl. Res. (2020). https://doi.org/10.1007/s13346-020-00802-8.

[63] B. Vaidya, N.S. Kulkarni, S.K. Shukla, V. Parvathaneni, G. Chauhan, J.K. Damon, A. Sarode, J.V. Garcia, N. Kunda, S. Mitragotri, V. Gupta, Development of inhalable quinacrine loaded bovine serum albumin modified cationic nanoparticles: Repurposing quinacrine for lung cancer therapeutics, International Journal of Pharmaceutics. 577 (2020) 118995. https://doi.org/10.1016/j.ijpharm.2019.118995.

www.manaraa.com

[64] S.K. Shukla, N.S. Kulkarni, P. Farrales, D.D. Kanabar, V. Parvathaneni, N.K. Kunda, A. Muth, V. Gupta, Sorafenib Loaded Inhalable Polymeric Nanocarriers against Non-Small Cell Lung Cancer, Pharm Res. 37 (2020) 67. https://doi.org/10.1007/s11095-020-02790-3.

[65] M.E. Abdelrahim, H. Chrystyn, Aerodynamic Characteristics of Nebulized Terbutaline Sulphate Using the Next Generation Impactor (NGI) and CEN Method, Journal of Aerosol Medicine and Pulmonary Drug Delivery. 22 (2009) 19–28. https://doi.org/10.1089/jamp.2008.0650.

[66] I. Takeuchi, Y. Taniguchi, Y. Tamura, K. Ochiai, K. Makino, Effects of l-leucine on PLGA microparticles for pulmonary administration prepared using spray drying: Fine particle fraction and phagocytotic ratio of alveolar macrophages, Colloids and Surfaces A: Physicochemical and Engineering Aspects. 537 (2018) 411–417. https://doi.org/10.1016/j.colsurfa.2017.10.047.

[67] S.K. Shukla, A. Chan, V. Parvathaneni, V. Gupta, Metformin-loaded chitosomes for treatment of malignant pleural mesothelioma – A rare thoracic cancer, International Journal of Biological Macromolecules. 160 (2020) 128–141. https://doi.org/10.1016/j.ijbiomac.2020.05.146.

[68] M.K. Kauffman, M.E. Kauffman, H. Zhu, Z. Jia, Y.R. Li, Fluorescence-Based Assays for Measuring doxorubicin in Biological Systems, React Oxyg Species (Apex). 2 (2016) 432–439. https://doi.org/10.20455/ros.2016.873.

[69] S.M. Chacko, K.G. Nevin, R. Dhanyakrishnan, B.P. Kumar, Protective effect of p-coumaric acid against doxorubicin induced toxicity in H9c2 cardiomyoblast cell

www.manaraa.com

lines, Toxicol Rep. 2 (2015) 1213–1221. https://doi.org/10.1016/j.toxrep.2015.08.002.

[70] Physical, Thermal, and Mechanical Properties of Polymers, in: Biosurfaces, John Wiley & Sons, Ltd, 2014: pp. 329–344. https://doi.org/10.1002/9781118950623.app1.

[71] M. Cooley, A. Sarode, M. Hoore, D.A. Fedosov, S. Mitragotri, A. Sen Gupta, Influence of particle size and shape on their margination and wall-adhesion: implications in drug delivery vehicle design across nano-to-micro scale, Nanoscale. 10 (2018) 15350–15364. https://doi.org/10.1039/C8NR04042G.

[72] D. Missirlis, R. Kawamura, N. Tirelli, J.A. Hubbell, Doxorubicin encapsulation and diffusional release from stable, polymeric, hydrogel nanoparticles, European Journal of Pharmaceutical Sciences. 29 (2006) 120–129. https://doi.org/10.1016/j.ejps.2006.06.003.

[73] B. Manocha, A. Margaritis, Controlled Release of Doxorubicin from Doxorubicin/-Polyglutamic Acid Ionic Complex, Journal of Nanomaterials. 2010 (2010) e780171. https://doi.org/10.1155/2010/780171.

[74] J. Ding, G. Xue, Q. Dai, R. Cheng, Glass transition temperature of polystyrene microparticles, Polymer. 34 (1993) 3325–3327. https://doi.org/10.1016/0032-3861(93)90412-4.

[75] J. Rieger, The glass transition temperature of polystyrene, Journal of Thermal Analysis. 46 (1996) 965–972. https://doi.org/10.1007/BF01983614.

www.manaraa.com

[76] A. Vigevani, M.J. Williamson, Doxorubicin, in: Analytical Profiles of Drug Substances, Elsevier, 1981: pp. 245–274. https://doi.org/10.1016/S0099-5428(08)60143-4.

[77] G. Das, A. Nicastri, M.L. Coluccio, F. Gentile, P. Candeloro, G. Cojoc, C. Liberale, F. De Angelis, E. Di Fabrizio, FT-IR, Raman, RRS measurements and DFT calculation for Doxorubicin, Microsc. Res. Tech. (2010) NA-NA. https://doi.org/10.1002/jemt.20849.

[78] Z.Q. Samra, S. Ahmad, M. Javeid, N. Dar, M.S. Aslam, I. Gull, M.M. Ahmad, ANTICANCER MEDICINES (DOXORUBICIN AND METHOTREXATE) CONJUGATED WITH MAGNETIC NANOPARTICLES FOR TARGETING DRUG DELIVERY THROUGH IRON, Preparative Biochemistry and Biotechnology. 43 (2013) 781–797. https://doi.org/10.1080/10826068.2013.782042.

[79] V. Hermán, H. Takacs, F. Duclairoir, O. Renault, J.H. Tortai, B. Viala, Core double–shell cobalt/graphene/polystyrene magnetic nanocomposites synthesized by in situ sonochemical polymerization, RSC Adv. 5 (2015) 51371–51381. https://doi.org/10.1039/C5RA06847A.

[80] J. Fang, Y. Xuan, Q. Li, Preparation of polystyrene spheres in different particle sizes and assembly of the PS colloidal crystals, Science China-Technological Sciences - SCI CHINA-TECHNOL SCI. 53 (2010) 3088–3093. https://doi.org/10.1007/s11431-010-4110-5.

[81] A.A.P. Mansur, S.M. Carvalho, Z.I.P. Lobato, M. de F. Leite, A. da S. Cunha, H.S. Mansur, Design and Development of Polysaccharide-Doxorubicin-Peptide

www.manaraa.com

Bioconjugates for Dual Synergistic Effects of Integrin-Targeted and Cell-Penetrating Peptides for Cancer Chemotherapy, Bioconjugate Chem. 29 (2018) 1973–2000. https://doi.org/10.1021/acs.bioconjchem.8b00208.

[82] J.S. Shankaranarayanan, J.R. Kanwar, A.J.A. AL-Juhaishi, R.K. Kanwar, Doxorubicin Conjugated to Immunomodulatory Anticancer Lactoferrin Displays Improved Cytotoxicity Overcoming Prostate Cancer Chemo resistance and Inhibits Tumour Development in TRAMP Mice, Scientific Reports. 6 (2016) 32062. https://doi.org/10.1038/srep32062.

[83] R. Sturm, A Computer Model for the Simulation of Nonspherical Particle Dynamics in the Human Respiratory Tract, Physics Research International. 2012 (2012) e142756. https://doi.org/10.1155/2012/142756.

[84] M. Shams, G. Ahmadi, H. Rahimzadeh, Transport and deposition of flexible fibers in turbulent duct flows, Journal of Aerosol Science. 32 (2001) 525–547. https://doi.org/10.1016/S0021-8502(00)00099-9.

[85] R. Sturm, W. Hofmann, A computer program for the simulation of fiber deposition in the human respiratory tract, Computers in Biology and Medicine. 36 (2006) 1252–1267. https://doi.org/10.1016/j.compbiomed.2005.07.004.

[86] T.B. Martonen, I.M. Katz, Deposition Patterns of Aerosolized Drugs Within Human Lungs: Effects of Ventilatory Parameters, Pharm Res. 10 (1993) 871–878. https://doi.org/10.1023/A:1018913311788.

[87] C. Darquenne, Aerosol Deposition in Health and Disease, J Aerosol Med Pulm Drug Deliv. 25 (2012) 140–147. https://doi.org/10.1089/jamp.2011.0916.

www.manaraa.com

[88] J. Wang, J. Bhattacharyya, E. Mastria, A. Chilkoti, A quantitative study of the intracellular fate of pH-responsive Doxorubicin-polypeptide nanoparticles, J Control Release. 260 (2017) 100–110. https://doi.org/10.1016/j.jconrel.2017.05.032.

[89] M. Li, Z. Tang, J. Lin, Y. Zhang, S. Lv, W. Song, Y. Huang, X. Chen, Synergistic antitumor effects of Doxorubicin-loaded carboxymethyl cellulose nanoparticle in combination with endostar for effective treatment of non-small-cell lung cancer, Adv Healthc Mater. 3 (2014) 1877–1888. https://doi.org/10.1002/adhm.201400108.

[90] L. He, H. Liang, L. Lin, B.R. Shah, Y. Li, Y. Chen, B. Li, Green-step assembly of low density lipoprotein/sodium carboxymethyl cellulose nanogels for facile loading and pH-dependent release of Doxorubicin, Colloids and Surfaces B: Biointerfaces. 126 (2015) 288–296. https://doi.org/10.1016/j.colsurfb.2014.12.024.

[91] T. Etrych, V. Subr, R. Laga, B. Říhová, K. Ulbrich, Polymer conjugates of Doxorubicin bound through an amide and hydrazone bond: Impact of the carrier structure onto synergistic action in the treatment of solid tumours, Eur J Pharm Sci. 58 (2014) 1–12. https://doi.org/10.1016/j.ejps.2014.02.016.

[92] Q. Gao, X. Han, J. Zhu, R. Chen, B. Sun, A polymer–drug conjugate for Doxorubicin: Synthesis and biological evaluation of pluronic F127-DOXorubicin amide conjugates, Journal of Applied Polymer Science. 124 (2012) 4953–4960. https://doi.org/10.1002/app.35613.

[93] Y. Yu, C.-K. Chen, W.-C. Law, H. Sun, P.N. Prasad, C. Cheng, A degradable brush polymer–drug conjugate for pH-responsive release of Doxorubicin, Polym. Chem. 6 (2015) 953–961. https://doi.org/10.1039/C4PY01194E.

www.manaraa.com

[94] S. Mahesh, K.-C. Tang, M. Raj, Amide Bond Activation of Biological Molecules, Molecules. 23 (2018). https://doi.org/10.3390/molecules23102615.

[95] M. Munerati, R. Cortesi, D. Ferrari, F. Di Virgilio, C. Nastruzzi, Macrophages loaded with Doxorubicin by ATP-mediated permeabilization: potential carriers for antitumor therapy, Biochim Biophys Acta. 1224 (1994) 269–276. https://doi.org/10.1016/0167-4889(94)90200-3.

[96] L. Wang, Y. Song, A. Parikh, P. Joyce, R. Chung, L. Liu, F. Afinjuomo, J.D. Hayball, N. Petrovsky, T.G. Barclay, S. Garg, DOXorubicin-Loaded Delta Inulin Conjugates for Controlled and Targeted Drug Delivery: Development, Characterization, and In Vitro Evaluation, Pharmaceutics. 11 (2019) 581. https://doi.org/10.3390/pharmaceutics11110581.

[97] M.P. Mohning, S.M. Thomas, L. Barthel, K.J. Mould, A.L. McCubbrey, S.C. Frasch, D.L. Bratton, P.M. Henson, W.J. Janssen, Phagocytosis of microparticles by alveolar macrophages during acute lung injury requires MerTK, American Journal of Physiology-Lung Cellular and Molecular Physiology. 314 (2017) L69–L82. https://doi.org/10.1152/ajplung.00058.2017.

[98] J.A. Champion, S. Mitragotri, Shape Induced Inhibition of Phagocytosis of Polymer Particles, Pharm Res. 26 (2009) 244–249. https://doi.org/10.1007/s11095-008-9626-z.

[99] N. Doshi, S. Mitragotri, Macrophages Recognize Size and Shape of Their Targets, PLoS One. 5 (2010). https://doi.org/10.1371/journal.pone.0010051.

[100] N. Chatterjee, J. Yang, S. Kim, S.W. Joo, J. Choi, Diameter size and aspect ratio as critical determinants of uptake, stress response, global metabolomics and epigenetic

www.manaraa.com

alterations in multi-wall carbon nanotubes, Carbon. 108 (2016) 529–540. https://doi.org/10.1016/j.carbon.2016.07.031.

[101] R.L. Siegel, K.D. Miller, A. Jemal, Cancer statistics, 2020, CA A Cancer J Clin. 70 (2020) 7–30. https://doi.org/10.3322/caac.21590.

[102] S. Haddadin, M.C. Perry, History of Small-Cell Lung Cancer, Clinical Lung Cancer. 12 (2011) 87–93. https://doi.org/10.1016/j.cllc.2011.03.002.

[103] J.D. Whitt, A.B. Keeton, B.D. Gary, L.A. Sklar, K. Sodani, Z.-S. Chen, G.A. Piazza, Sulindac sulfide selectively increases sensitivity of ABCC1 expressing tumor cells to doxorubicin and glutathione depletion, J Biomed Res. 30 (2016) 120–133. https://doi.org/10.7555/JBR.30.20150108.

[104] A. Sampson, B.G. Peterson, K.W. Tan, S.H. Iram, Doxorubicin as a fluorescent reporter identifies novel MRP1 (ABCC1) inhibitors missed by calcein-based high content screening of anticancer agents, Biomedicine & Pharmacotherapy. 118 (2019) 109289. https://doi.org/10.1016/j.biopha.2019.109289.

[105] Y. He, K. Park, Effects of the Microparticle Shape on Cellular Uptake, Mol. Pharmaceutics. 13 (2016) 2164–2171. https://doi.org/10.1021/acs.molpharmaceut.5b00992.

[106] S.E.A. Gratton, P.A. Ropp, P.D. Pohlhaus, J.C. Luft, V.J. Madden, M.E. Napier, J.M. DeSimone, The effect of particle design on cellular internalization pathways, PNAS. 105 (2008) 11613–11618. https://doi.org/10.1073/pnas.0801763105.

[107] S. Wu, X. Yang, Y. Li, H. Wu, Y. Huang, L. Xie, Y. Zhang, Z. Hou, X. Liu, Preparation of HCPT-Loaded Nanoneedles with Pointed Ends for Highly Efficient

www.manaraa.com

Cancer Chemotherapy, Nanoscale Res Lett. 11 (2016). https://doi.org/10.1186/s11671-016-1491-9.

[108] N. Koundouros, G. Poulogiannis, Reprogramming of fatty acid metabolism in cancer, British Journal of Cancer. 122 (2020) 4–22. https://doi.org/10.1038/s41416-019-0650-z.

[109] M. Sok, M. Šentjurc, M. Schara, Membrane fluidity characteristics of human lung cancer, Cancer Letters. 139 (1999) 215–220. https://doi.org/10.1016/S0304-3835(99)00044-0.

[110] E.C. Costa, A.F. Moreira, D. de Melo-Diogo, V.M. Gaspar, M.P. Carvalho, I.J. Correia, 3D tumor spheroids: an overview on the tools and techniques used for their analysis, Biotechnology Advances. 34 (2016) 1427–1441. https://doi.org/10.1016/j.biotechadv.2016.11.002.

[111] G. Mehta, A.Y. Hsiao, M. Ingram, G.D. Luker, S. Takayama, Opportunities and challenges for use of tumor spheroids as models to test drug delivery and efficacy, Journal of Controlled Release. 164 (2012) 192–204. https://doi.org/10.1016/j.jconrel.2012.04.045.

[112] A.S. Nunes, A.S. Barros, E.C. Costa, A.F. Moreira, I.J. Correia, 3D tumor spheroids as in vitro models to mimic in vivo human solid tumors resistance to therapeutic drugs, Biotechnology and Bioengineering. 116 (2019) 206–226. https://doi.org/10.1002/bit.26845.

[113] P. Benien, A. Swami, 3D tumor models: history, advances and future perspectives, Future Oncol. 10 (2014) 1311–1327. https://doi.org/10.2217/fon.13.274.

المنارة للاستشارات
www.manaraa.com

[114] Y. Imamura, T. Mukohara, Y. Shimono, Y. Funakoshi, N. Chayahara, M. Toyoda, N. Kiyota, S. Takao, S. Kono, T. Nakatsura, H. Minami, Comparison of 2D- and 3D-culture models as drug-testing platforms in breast cancer, Oncol. Rep. 33 (2015) 1837–1843. https://doi.org/10.3892/or.2015.3767.

[115] R. Agarwal, P. Jurney, M. Raythatha, V. Singh, Sidlgata.V. Sreenivasan, L. Shi, K. Roy, Effect of Shape, Size, and Aspect Ratio on Nanoparticle Penetration and Distribution inside Solid Tissues Using 3D Spheroid Models, Adv. Healthcare Mater. 4 (2015) 2269–2280. https://doi.org/10.1002/adhm.201500441.

[116] Y.-R. Zhang, R. Lin, H.-J. Li, W. He, J.-Z. Du, J. Wang, Strategies to improve tumor penetration of nanomedicines through nanoparticle design, WIREs Nanomed Nanobiotechnol. 11 (2019) e1519. https://doi.org/10.1002/wnan.1519.

[117] K.C.L. Black, Y. Wang, H.P. Luehmann, X. Cai, W. Xing, B. Pang, Y. Zhao, C.S. Cutler, L.V. Wang, Y. Liu, Y. Xia, Radioactive 198Au-doped nanostructures with different shapes for in vivo analyses of their biodistribution, tumor uptake, and intratumoral distribution, ACS Nano. 8 (2014) 4385–4394. https://doi.org/10.1021/nn406258m.

[118] A. Garapaty, J.A. Champion, Tunable particles alter macrophage uptake based on combinatorial effects of physical properties, Bioeng Transl Med. 2 (2017) 92–101. https://doi.org/10.1002/btm2.10047.

[119] W.-B. Chung, H.-J. Youn, Pathophysiology and preventive strategies of anthracycline-induced cardiotoxicity, Korean J Intern Med. 31 (2016) 625–633. https://doi.org/10.3904/kjim.2016.017.

www.manaraa.com

[120] M. Dallons, C. Schepkens, A. Dupuis, V. Tagliatti, J.-M. Colet, New Insights About doxorubicin-Induced Toxicity to Cardiomyoblast-Derived H9C2 Cells and Dexrazoxane Cytoprotective Effect: Contribution of In Vitro 1H-NMR Metabonomics, Front Pharmacol. 11 (2020). https://doi.org/10.3389/fphar.2020.00079.

www.manaraa.com

Vita

Name	*Snehal Shukla*
Baccalaureate Degree	*Bachelor of Pharmacy*, *Institute of Pharmacy, Nirma University, Ahmedabad*
Date Graduated	*May,2012*
Other Degrees and Certificates	*Master of Pharmacy, National Institute of Pharmaceutical Education and Research , Ahmedabad,* *Major: Pharmaceutical Analysis*
Date Graduated	*June,2014*

www.manaraa.com